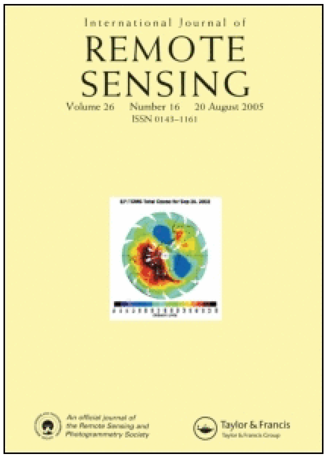

International Journal of Remote Sensing
Publication details, including instructions for authors and subscription information:
http://www.informaworld.com/smpp/title~content=t713722504

Calibration of the AVHRR visible and near-IR bands by atmospheric scattering, ocean glint and desert reflection

Y. J. Kaufman [a]; B. N. Holben [b]
[a] Laboratory for Atmospheres, code 913, NASA/Goddard Space Flight Center, Greenbelt, MD, U.S.A.
[b] Laboratory for Terrestrial Physics, NASA/Goddard Space Flight Center, Greenbelt, MD, U.S.A.

Online Publication Date: 01 January 1993
To cite this Article: Kaufman, Y. J. and Holben, B. N. (1993) 'Calibration of the AVHRR visible and near-IR bands by atmospheric scattering, ocean glint and desert reflection', International Journal of Remote Sensing, 14:1, 21 - 52
To link to this article: DOI: 10.1080/01431169308904320
URL: http://dx.doi.org/10.1080/01431169308904320

INT. J. REMOTE SENSING, 1993, VOL. 14, NO. 1, 21-52

Calibration of the AVHRR visible and near-IR bands by atmospheric scattering, ocean glint and desert reflection

Y. J. KAUFMAN

Laboratory for Atmospheres, code 913, NASA/Goddard Space Flight Center, Greenbelt, MD 20771, U.S.A.

and B. N. HOLBEN

Laboratory for Terrestrial Physics, NASA/Goddard Space Flight Center, Greenbelt, MD 20771, U.S.A.

(Received 5 October 1990: in final form 26 April 1991)

Abstract. An inflight calibration for AVHRR visible and near-IR bands is discussed and applied to NOAA-7, NOAA-9 and NOAA-11 from 1981 to 1990. The approach, independent of ground support, relies on three unique earth–atmosphere phenomena: molecular scattering over the ocean for absolute visible band calibration, ocean glint to transfer the calibration from the visible band to the near-IR band, and desert reflectance to monitor, independently, the stability of the visible and near-IR bands. The resulting two calibration methods differ in the brightness range and spectral response of the radiance source (molecular scattering versus desert reflectance). Both methods agreed on calibration deterioration for NOAA-9 of 10 ± 3 per cent in the visible band and 16 ± 2 per cent in the near-IR shortly after launch, and 22 ± 2 per cent in both bands three years later. The ocean method showed an increase of 6 per cent and 9 per cent in the sensitivity of the visible and near-IR bands respectively over the lifetime of NOAA-7. However, the desert method showed a decrease of 10 and 12 per cent, respectively, in the two bands. Possible reasons for the differences between the resultant calibration for NOAA-7 from the two methods are discussed. NOAA-11 was calibrated using the desert radiances only. Its inflight response was lower from the preflight response by 21 per cent in channel 1 and 33 per cent in channel 2, a short time after launch. Recommendations for the absolute calibration of NOAA-7, -9 and -11 are given for channels 1 and 2 as a function of time and are compared with other published AVHRR calibrations. The calibration deterioration results in a change in the vegetation index (NDVI) between 0·0 and 0·09. A simple correction scheme is suggested for uncorrected NOAA-7, -9 and -11 NDVI and implications of the calibration ratio on AVHRR remote sensing are discussed.

1. Introduction

Interest in radiometric calibration of the earth viewing satellites has developed mainly in the last several years, stimulated with the capability to utilize quantitative radiometry (Price 1987 a). The early products of satellite imagery of the Earth's surface, consisted of qualitative images. The first quantitative assessments were based on supervised and unsupervised classification, that did not require radiometric calibration. Currently there is an increasing effort to improve the quality of quantitative information obtained from the satellite imagery. Corrections for the atmospheric effect are being developed (Diner and Martonchik 1985, Kaufman and Sendra 1988), and special care is devoted to remote sensing products (e.g., the vegetation index) that are less dependent on the direction of observation or the solar zenith angle (Holben and Fraser 1984, Holben 1986), but are affected by the atmosphere and by the uncertainty in the sensor calibration. This emphasis on quantitative data is a result of application of the satellite imagery to acquire information on long term variation in land and atmospheric processes, e.g., vegetation (Tucker *et al.* 1985) and clouds (Arking and Childs 1985). These long term data sets are required, for example, in order to assess the impact of the human activity on climate change, and other changes in the environment.

The calibration of satellite sensors in the solar spectrum is difficult due to lack of reliable inflight calibration devices. The preflight calibration may change in space due to the different environment surrounding the instrument in space; e.g., outgassing, bombardment by energetic particles from space, variation in the filter transmittance and spectral response, and slow deterioration of the electronic system. As a result there is a need for an independent method for inflight sensor calibration, that in addition to providing an updated calibration, can be an indication of the quality of the performance of the system. One such method is to fly an aircraft with a calibrated radiometer that measures the spectral radiance of the target observed by the satellite in the same illumination and observation directions (Hovis and Knoll 1985, Smith *et al.* 1987, 1988). Although this may be the most direct method, it is relatively expensive, complex and cannot be used to calibrate historical data. The method presented here is used to calibrate the sensor by using well-known physical characteristics of the atmosphere, ocean and deserts, as well as the digital satellite imagery.

1.1. *Calibration over ocean*

Radiances over remote ocean areas were used to calibrate satellite sensors (Koepke 1982, Fraser and Kaufman 1986). Koepke (1982) used ground measurements in a given location to calibrate the Meteosat sensor. Fraser and Kaufman (1986) used four years of GOES-VISSR imagery over different remote ocean areas (without ground measurements), to calibrate the sensor (see figure 1). The method used in the present investigation is based on measurements by the AVHRR of the radiance over the ocean, out of the glint direction. Over the ocean, for satellite view zenith angles of 50°–70° (view zenith angle is the angle between the line of sight and the perpendicular to the Earth's surface at the observed point), in the backscattering direction, 70–80 per cent of the radiance originates from molecular scattering that is practically invariant in time and space (see table 1). It depends only on the atmospheric pressure and is given by Rayleigh's (1871) formulation. The rest 20–30 per cent are due to aerosol scattering, foam reflectivity and underwater reflectance. The time dependence of the gain of the GOES-VISSR sensor, calibrated by this method (see Fraser and Kaufman, 1986 and figure 1) showed the clear difference between the characteristics of the sensor of the old satellite before replacement (in August 1981) and the new sensor (after August 1981). The gain sequence of the new sensor showed that the uncertainty in the precision of the calibration method combined with fluctuations in the sensor gain were only ± 2 per cent. Before replacement in August 1981, the deteriorating VISSR sensor system combined with gain changes induced by commands from the ground, resulted in the strong gain fluctuations shown in figure 1.

1.2. *Calibration over deserts*

Radiance over desert areas, has been used to monitor the satellite calibration. Frouin and Gautier (1987) and Teillet *et al.* (1988, 1990) used the White Sands National Monument in New Mexico to calibrate the visible and near-IR satellite sensors. This area receives relatively little rain (Price, 1987 a) and is usually under a clear atmosphere, but may suffer from variation in soil moisture (Frouin and Gautier 1987) and in shifting dunes. Desert areas that are invariable in time, in dry cloudless conditions can be used to monitor the stability of the calibration (Staylor, 1986, Kaufman *et al.* 1990, Staylor 1990, Holben *et al.* 1990). In order to use the desert also for an absolute calibration, the desert reflectance must be determined for particular instances. Teillet *et al.* (1990) used ground measurements of the surface reflectance and the high resolution Landsat Thematic Mapper to derive the surface reflectance during the AVHRR observation. Frouin and Gautier (1987) used laboratory measurements of the White Sands reflectivity as the basis for the satellite calibration. An additional problem of desert areas is the angular dependence of their reflectance. For example, the presence of dunes, such as the White Sands National Monument, not the alkali flat area at White Sands, give rise to a strong non-Lambertian appearance. The observation direction changes between the different

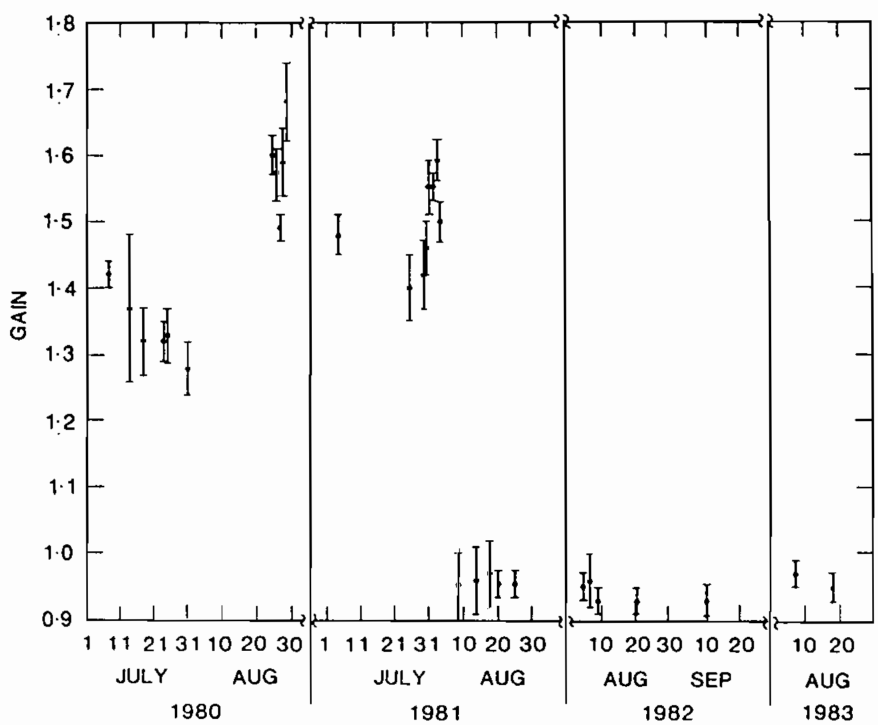

Figure 1. The gain for the GOES-VISSR stationed at 75° W (after Fraser and Kaufman 1986). The gains are computed by calibrating the sensor by the radiance detected over remote ocean areas, far from the glint, at slant directions of observation. Note that at 9 August 1981 the gain is changed from a high and irregular value to close to 1 and very regular due to a replacement of the stationed satellite with a new one (a high gain corresponds to a low sensor response).

Table 1. The relative contribution to the upward radiance of molecular scattering, aerosol scattering (for optical thickness of 0·1 in Band 1 and 0·08 in Band 2), underwater reflectance and glint (for solar zenith angle of 40°). The radiance (L) is normalized by ($L^N = \pi L/E_o$) where E_o is the extraterrestrial solar flux. Computations are done with the radiative transfer code of Ahmad and Fraser (1982) for $V = 5\,\mathrm{m\,s^{-1}}$.

Band/ wave-length (μm)	View zenith angle	Azimuth angle	Contribution to the upward radiance L^N and (%)				
			Under-water and foam	Glint	Aerosol scattering	Molecular scattering	Total
1	70	180	0·0019	no glint	0·0128	0·0496	0·0643
0·63			(3%)	(0%)	(20%)	(77%)	(100%)
1	30	180	0·0018	no glint	0·0065	0·0176	0·0259
0·63			(7%)	(0%)	(25%)	(68%)	(100%)
1	50	0	0·0019	0·191	0·0079	0·251	0·226
0·63			(1%)	(85%)	(3%)	(11%)	(100%)
2	70	180	0·0010	no glint	0·0085	0·0153	0·0248
0·82			(4%)	(0%)	(34%)	(62%)	(100%)
2	50	0	0·0009	0·186	0·0060	0·0087	0·202
0.82			(1%)	(92%)	(3%)	(4%)	(100%)

satellite overpasses, and the solar zenith angle varies from one overpass to the next one, due to variation in the subsatellite point. The solar zenith angle for AVHRR, also drifts from year to year, due to a delay of 0·5 hour/year^{-1} in the satellite local time of overpass. Therefore, though dessert areas may provide a unique capability for testing the stability of the satellite calibration, they must be used with caution, with special emphasis on the view and illumination directions (Kaufman *el al.* 1990, Staylor 1990, Holben *et al.* 1990). Several desert areas are needed in order to distinguish between variations in the surface/atmosphere and sensor characteristics. Our choice of the desert sites for calibration is similar to that of Staylor (1986, 1990), that found that in lower latitudes, deserts (and mainly the Libyan desert) best met the requirements of long term stability, low solar zenith angle and therefore and precipitation.

Recently, Brest and Rossow (1990) used scatter diagrams of radiances detected over many surface covers from all over the world, under a variety of measurement conditions to detect calibration change. By this method, the large quantity of data may smooth random local fluctuations in the surface reflectance and in the atmospheric conditions, and result in calibration coefficients that are averaged over surfaces with several spectral characteristics. However, there are two main problems with the approach of Brest and Rossow (1990). They have to assume that in average the Earth's surface reflectance and the atmosphere are not changing from year to year. As a result any climate change, or climate fluctuations, would manifest themselves in the calibration. Such changes can result from climate variations that affect the surface reflectance (e.g. vegetation); variation in unscreened subpixel clouds; variation in the concentration of air pollution, that can change the reflected light. The second problem is a systematic error in the calibration due to the continuous drift in the satellite equatorial crossing time, of 0·5 hr/year^{-1}. This drift is expected to result in observation of a more cloudy area, with more reflective haze.

The subsequential increase in the solar zenith angle is expected to result in a larger surface reflectance. Selection of specific desert areas in low latitude (Staylor 1986, Kaufman *et al.* 1990, Staylor 1990, Holben *et al.* 1990), using only nadir data and screening individually the images for clouds, has a much higher potential for successful calibration.

In this paper three independent Earth and atmospheric phenomena are used to callibrate the AVHRR: molecular scattering in the atmosphere over the ocean, sun glint and desert reflectance. In addition, view of the deep space is used to monitor the calibration offset. Molecular scattering over the ocean provides a stable absolute calibration signal, useful for the visible band calibration of the AVHRR as it was applied previously to calibrate the GOES VISSR sensor (Fraser and Kaufman 1986). Since the molecular scattering is much weaker in the near-IR (see table 1), ocean glint is used to transfer the calibration of the visible band to the near-IR band, owing to the spectral independence of the glint. We do not apply the calibration over the ocean using molecular scattering for Band 2, since the molecular scattering contribution to the radiance in this band is significantly smaller than in Band 1 (see table 1). Calibration over desert areas is used to monitor independently, the stability of the calibration of the visible and near-IR bands. These methods do not require ground support, therefore they can be applied to present as well as historical data, using independent sites all over the world.

2. The method

In this section we shall describe the calibration method applied to the NOAA-7, NOAA-9 and NOAA-11 sensors. The method is applied to the 4 km resolution AVHRR data (GAC). The following notations are used in the calibration process. The relation between the spectral radiance (L_i) detected by the sensor in band i and the integer count value on a data tape (C_i) is :

$$L_i = \alpha_i (C_i - C_{oi}) \qquad (\mathrm{W\,m^{-2}\,sr^{-1}\,\mu m^{-1}}) \tag{1}$$

where α_i is the calibration coefficient and C_{oi} is the deep space count for band *i*. The radiance L_i can be normalized to reflectance units:

$$L_i^N = \pi L_i d^2 / E_{oi} \tag{2}$$

where *d* is the Sun-Earth distance in astronomical units E_{oi} is the solar exoatmospheric band average solar irradiance for $d = 1$ ($\mathrm{W\,m^{-2}\,\mu m^{-1}}$). The normalized radiance L_i^N is equal to the surface reflectance for no atmosphere and for Sun at zenith. The calibration equation for L_i^N is:

$$L_i^N = \gamma_i (C_i - C_{oi}) \qquad \text{where} \quad \gamma_i = \alpha_i \pi d^2 / E_{oi} \tag{3}$$

The change in the sensor calibration (r_i) between the true γ_i(true) and the preflight γ_i(preflight) calibration coefficients is given by the calibration ratio:

$$r_i = \gamma_i(\text{preflight}) / \gamma_i(\text{true}) \tag{4}$$

The preflight calibration coefficient is given on the magnetic tapes supplied by NOAA.

2.1. *Deep space values*

The deep space values measured by the sensor and the NOAA preflight offsets were obtained from the NOAA magnetic tapes and are tabulated in table 2. The

Table 2. Deep space values used in the calibration.

Satellite	Year	Preflight offset		Deep space	
		Band 1	Band 2	Band 1	Band 2
NOAA-7	1981	32·2	32·6	36·0	38·0
NOAA-7	1982	32·2	32·6	36·0	37·7
NOAA-7	1983	32·2	32·6	35·8	37·4
NOAA-7	1984	32·2	32·6	35·4	37·2
NOAA-9	1985	36·2	36·1	38·0	39·9
NOAA-9	1986	36·2	36·1	37·9	39·3
NOAA-9	1987	36·2	36·1	37·8	39·1
NOAA-9	1988	36·2	36·1	37·8	39·0
NOAA-11	1989	41·2	41·0	40·0	40·0
NOAA-11	1990	41·2	41·0	40·0	40·0
NOAA-11	1991	39·8	40·0	40·0	40·0

deep space values did not change substantially with time. They were subtracted from the digital counts, thus the calibration from here on consists from the derivation of the coefficients α_i or γ_i (1) or (3). The preflight vlaues of α_i are reported by Price (1987 b, 1988) and given in appendix A1.

2.2. *Calibration over the oceans*

The upward radiance above remote ocean areas is composed of the underwater reflectance, reflection from the water-air interface, molecular scattering in the atmosphere and aerosol scattering (see figure 2). For a cloudless air mass with a small amount of haze and far from the ocean glint, the major contribution (70–80

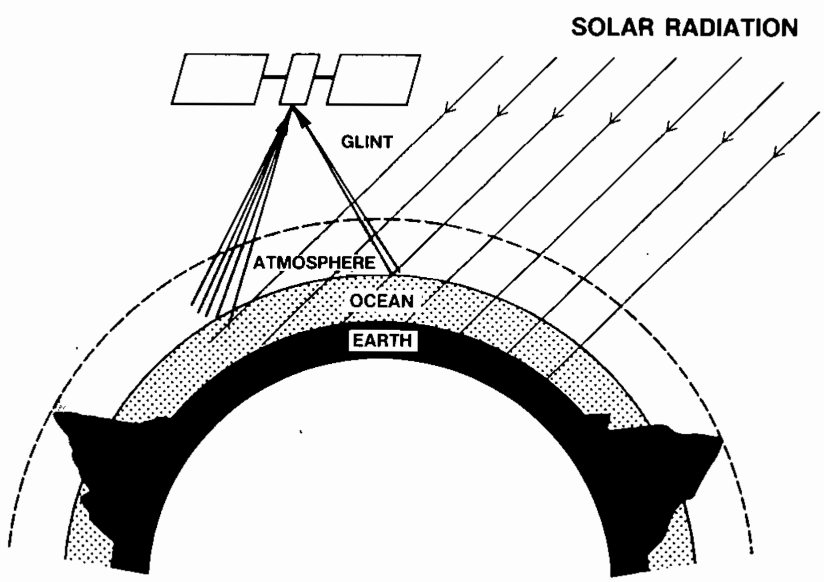

Figure 2. Schematic diagram of the calibration signal over the ocean.

per cent) to the upward radiance in the visible part of the spectrum is from molecular scattering in the atmosphere (see Fraser and Kaufman 1986 and table 1). The contribution of the underwater light, reflection of sunlight and skylight and the aerosol scattering is accounted for by an appropriate radiative transfer program (Ahmad and Fraser 1982). The model accounts for aerosol and molecular multiple scattering as well as effects of polarization and rough ocean reflection. The contribution of molecular scattering to the upward radiance is maximal at slant directions of observations, and far from the glint direction. The model assumes a plane parallel atmosphere, which for the maximum view zenith angle of 72° introduces an error in the air mass of 0·6 per cent due to the Earth's sphericity (Jursa 1985). A similar error is expected in the computed radiance. Figure 3, shows the dependence of the radiance detected by the satellite on the view angle in the principal plane. The radiance for azimuth of 180° increases with the increase of the view angle, due to the increase of atmospheric scattering. The figure shows both radiance detected by the AVHRR in band 1 and 2, as well as the temperature (Band 4). Irregularities in the temperature can indicate the presence of clouds. This is especially important over the bright glint, where thin clouds cannot be detected otherwise. In figure 4 the radiances in Bands 1 and 2 are compared with theoretical

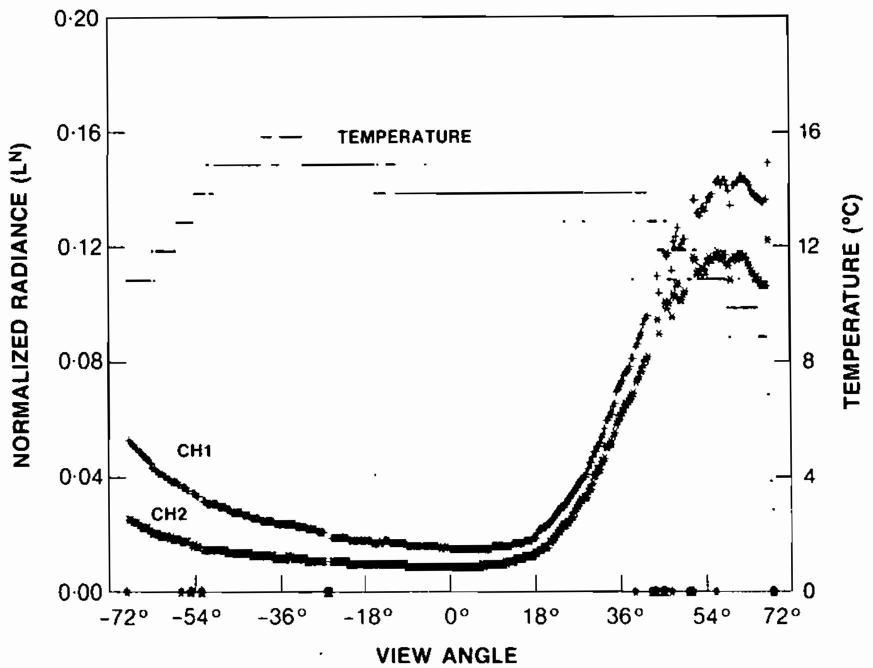

Figure 3. The radiance, in bands 1 (+) and 2 (*) (normalized by $L^N = \pi L/E_o$, where E_o is the extraterrestrial solar flux), detected by the satellite using the calibration provided on the digital tape, and the temperature based on Band 4. The data were acquired on 30 December 1987, around lat. 12° S and long. 100° E and are plotted as a function of the view angle (relative to the normal surface). The azimuth between the view direction and the solar rays is 14° on the right part of the figure and 166° on the left part. Data points that are eliminated in the screening process are marked on the bottom of the figure. The temperature (·) is also shown.

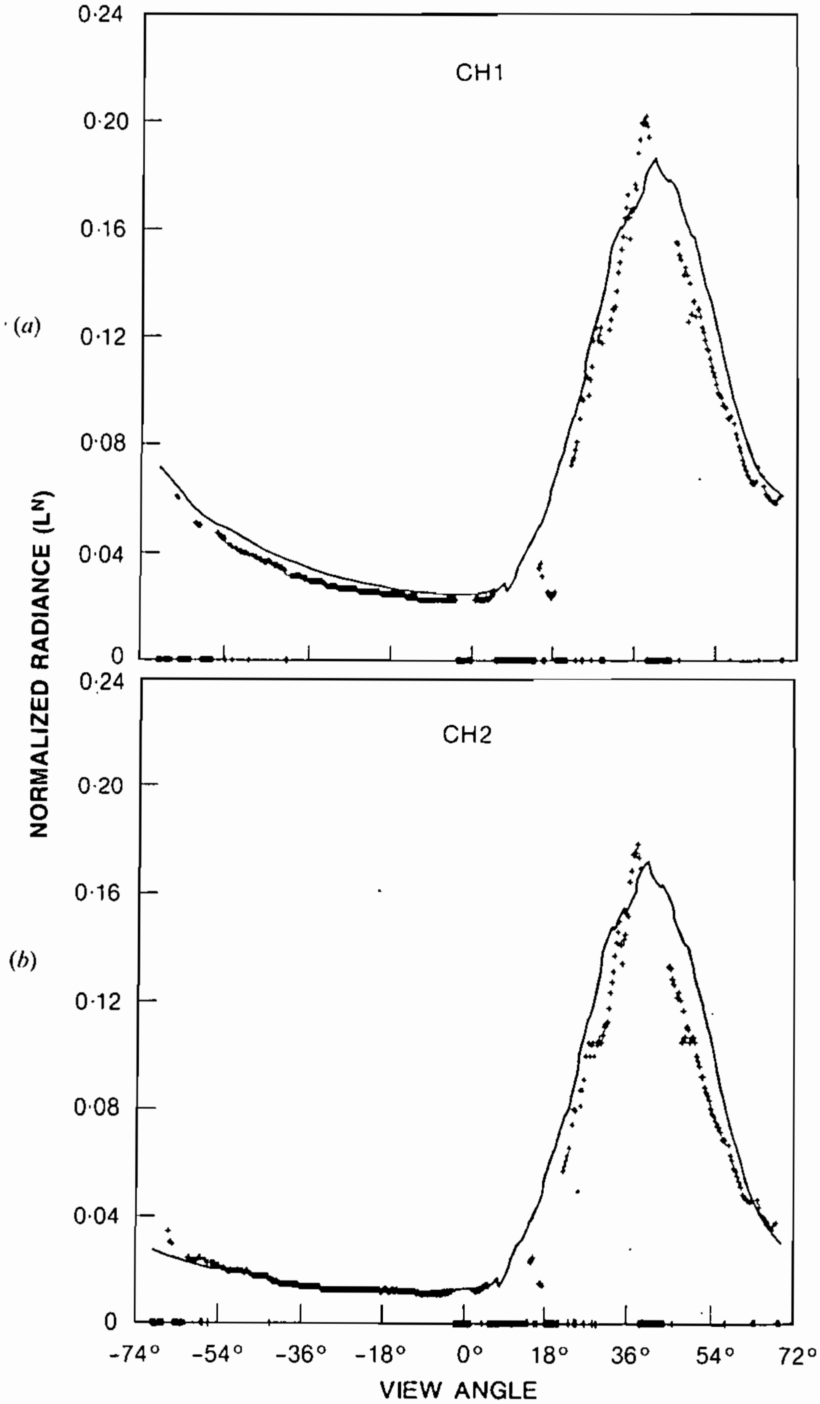

Figure 4. The radiance (normalized by $L^N = \pi L/E_o$) in Band 1 (*a*) and Band 2 (*b*), detected by the satellite using the calibration provided on the tape (+) and the theoretical predictions (——). The data were acquired on 1 December 1985, around lat. 20° S and long. 110° E and are plotted as a function of the view zenith angle. The azimuth between the view direction and the solar rays is 1° on the right part of the figure and 179° on the left part.

computations. The radiances are computed for aerosol optical thickness of 0·10 in band 1 and 0·08 in Band 2, for a maritime aerosol (Fraser and Kaufman 1986). The underwater reflectance is 0·003 in Band 1 and 0·0 in Band 2, and the surface wind is $5\,\mathrm{m/s^{-1}}$. The Rayleigh scattering optical thickness, the ozone absorption in Band 1 and the water vapour absorption in Band 2 were computed using a weighted average of the values on the spectral irradiance in each band. Details are given in appendix A1.

Approximately 87 per cent of the glint radiance is due to the specular reflection (see table 1). This reflection cannot be theoretically established with the same accuracy as the molecular scattering, since it depends on the wind speed and the wave structure, but it is independent of the radiation wavelength, and therefore, can be used to determine the relative calibration of Band 2 to Band 1 for reflectance range of 0·1–0·3. This transfer of the calibration from Band 1 to Band 2, is accomplished by comparison of the ratio between the measured normalized radiances in the two bands over the glint, with theoretical prediction of the ratio. The calibration ratio between Bands 1 and 2 is therefore, determined from:

$$\frac{r_1}{r_2}=\frac{\gamma_1(\text{preflight})}{\gamma_1(\text{true})}\bigg/\frac{\gamma_2(\text{preflight})}{\gamma_2(\text{true})}=\frac{\gamma_1(\text{preflight})(C_1-C_{01})}{\gamma_2(\text{preflight})(C_2-C_{02})}\bigg/\frac{L_1^N}{L_2^N} \tag{5}$$

The theory takes into account the different atmospheric effect on the radiance in the two bands (the details of the calibration are given in appendix A1). The glint angular width depends on the wind speed; which, therefore, can be estimated from it. Wind speed is used to eliminate data with high wind speeds, that may be accompanied with significant amount of white caps. The wind speed used in the theoretical computations (as is in figure 4) is $V=5\,\mathrm{m/s^{-1}}$. The actual wind speed is not required in the calibration, since it does not affect the radiance far from the glint, and does not affect the spectral dependence of the radiance at the glint (although it affects its magnitude).

2.2.1. *Data screening*

In order to reduce the effect of clouds on the calibration accuracy to a minimum a data screening algorithm must be applied. The following are the steps of the data screening:

1. Choose an area for calibration that is visually with a minimal amount of clouds. An area of 50 lines was chosen here.
2. From each group of pixels (e.g. 50 pixels) taken for the same view direction choose a subgroup of pixels (e.g. 10 pixels) with minimal brightness in Band 1. For the calibration (e.g. the data in figure 3) the average of this group (except the darkest pixel) is used. The darkest pixel is ignored in order to avoid a possible erroneous zero value. The difference between the darkest and brightest pixel in this subgroup is used to determine if the group is cloud-free. For azimuth ϕ (between the line of view and the solar rays) of $\phi>90°$ (backscattering) the difference is restricted to 1 count or less (corresponding to a change in the surface reflectance of 0·001 or less). For azimuth $\phi\leqslant 90°$, which may be affected by the glint, the difference is restricted to be less than 10 per cent of the radiance.
3. For the data set obtained from steps 1–2 check the temperature profile across the image. Temperature nonuniformities (except a decrease in the temperature

for view near the horizon) may show the presence of clouds, that may not be detected in step 1, or the presence of different air masses (e.g., dry and wet, hazy and clear), covering the image, that may result in atmospheric nonuniformities. Figure 5 shows an example of cloud detection. Around view angle of $-18°$ the data were screened for clouds in step 2, and therefore, the data in Band 1 and 2 were nullified. The clouds over the glint (view angle $> 54°$) were not detected in step 2 but can be seen from the lower temperatures. Thus, the glint data of figure 5 were not used.

2.3. *Calibration over desert areas*

The method used for calibration of the sensor over desert areas is a direct function of the criteria we place on the optical properties of the site and overlying atmosphere. The site must be bright (reflectance 0·2–0·4), so that the atmospheric effect on the upward radiance will be minimal (see Fraser and Kaufman 1985), large, uniform spatially and temporally, and as close to isotropic as possible. The overlying atmosphere must be free of clouds, dust outbreaks and anthropogenic aerosols and the existing aerosols and water vapour must be distributed uniformly and temporally constant. Testing several sites from all over the world, we narrowed our choice to four sites in the north of the Sahara, in the vicinity, and inside the Libyan desert site of Staylor (1990). The chosen sites are flat, devoid of vegetation, sand covered, geologically stable and not altered by man or animals. Lacking ground observations to check these criteria, we have detailed the influence of each of these on the satellite

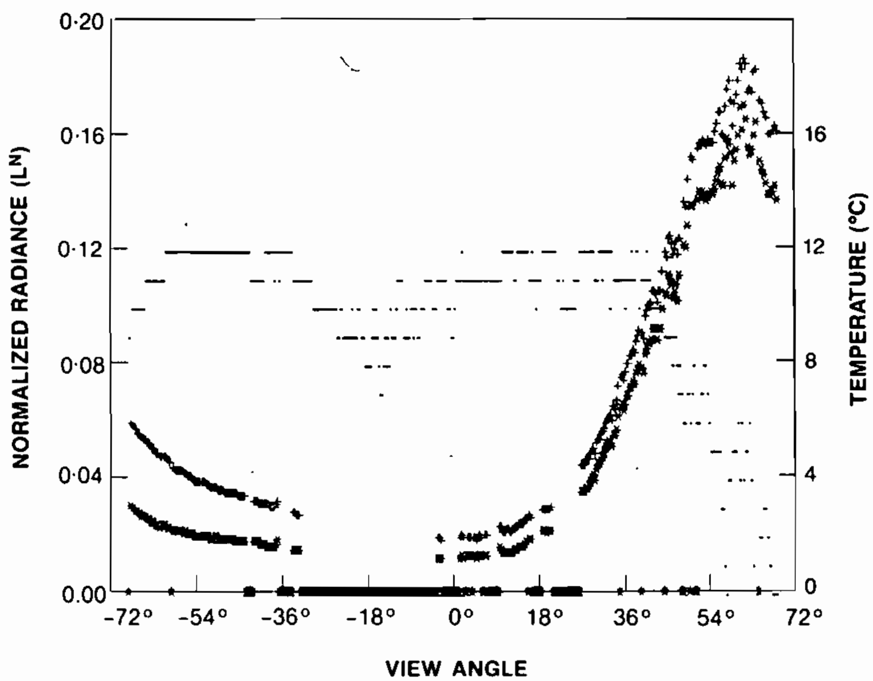

Figure 5. Same as figure 3 except for 14 December 1987, which shows the effect of clouds on the temperature and on data screening.

measured response as a function of viewing and illumination geometry in appendix A2.

The four chosen calibration sites have a reflectance of approximately 0·4. We have chosen desert sites approximately 100 km square from which we can generate a standard deviation necessary for examining spatial uniformity of the surface and atmosphere. Near-nadir view data observations are processed for August and September of each year, for every 9-day repeat cycle. The main differences between the present desert calibration and the calibration of Staylor (1990) are the following:

(*a*) Four smaller sites were presently selected, rather than one large site, in order to be able to compare the results of calibration for different sites, and to facilitate an easy visual cloud discrimination.
(*b*) Only data from a short period of time each year were used (e.g., August and September for NOAA-7 and -9) in order to minimize the variation of the solar zenith angle and to choose a period of the year when cloudiness and humidity are minimal.

Figure 6 shows an example for such data for the reflectance over the Egyptian desert (area 2) as a function of the day of the year for 1981–1988. The 9-day repeat cycle minimizes variations in the reflectances detected by the AVHRR due to changes in viewing (0–25°—see figure 7) and illumination (30–60°—see figure 7 and appendix A2 for details) directions and allows enough samples to evaluate the temporal uniformity of the surface and atmosphere.

The method of calibration follows: for a given date, the 4 km resolution GAC pixels are selected for the calibration site in Bands 1 and 2. A cosine correction of the solar zenith angle is made for each file. The mean and standard deviation is calculated for each band. If the standard deviation is less than 2 per cent of the mean value, the data are retained as part of the calibration data set (see appendix A2 for justification of this limit). This part of the procedure is also interactive and can involve the thermal band for cloud detection. Data is again selected for observation 9-days later and the above procedure is repeated for both bands. After the August and September data sets have been completed, overall means and standard deviations are calculated for both bands and represent the calibration values for that year, for a given site. Multi-year data sets are then created and presented as the desert calibration results.

2.4. *Accuracy and characteristics of the calibration methods*

The calibration methods calibrate Band 1 over the ocean in the range of surface reflectance of 0·02–0·09. The transfer of the calibration to Band 2 by the ocean glint is for the range of reflectances of 0·1–0·3. Desert radiances are used to measure the degradation in the calibration for reflectance around 0·4. Due to the intrinsic linearity of the detector, the calibration over the ocean and deserts can be extrapolated or interpolated to the rest of the radiometric range of the sensor. The zero offset of the sensor is found for each image from the deep space values recorded on the magnetic tape (together with the image) and is accounted for (see table 2). The absolute error in the calibration over the oceans for Band 1 is expected to be ± 10 per cent (for a 50 per cent uncertainty in the aerosol scattering optical thickness and optical properties) and the precision ± 8 per cent for each individual point, and ± 5 per cent for an ensemble of calibration values. This error is mainly due to uncertainty in the aerosol optical thickness. Calibration of Band 2 is based on the

(a)

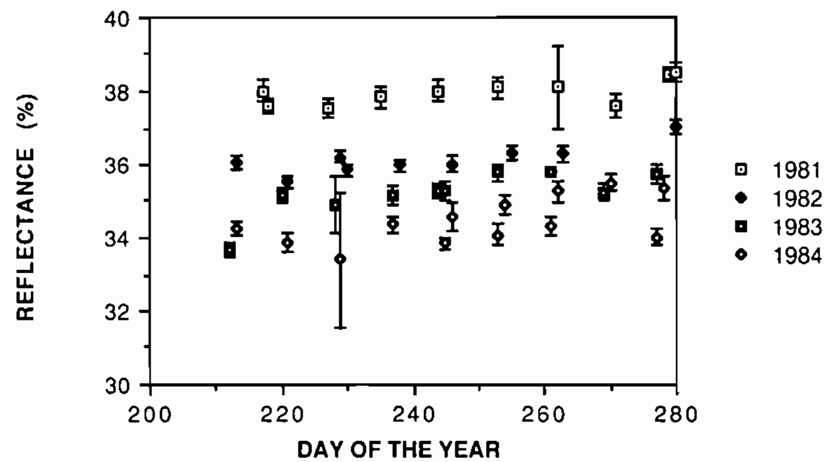

(b)

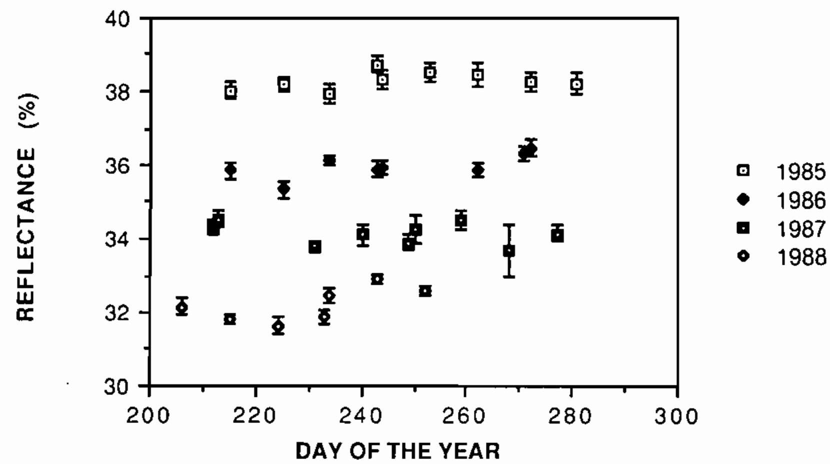

Figure 6. Reflectance over the Egyptian desert (area no. 2) as detected by the AVHRR sensor (defined as L^N/μ_o) and calibrated with the coefficients given on the magnetic tape. The reflectances are given as a function of time for Band 1, for NOAA-7 (top plot) and NOAA-9 (bottom plot). The data were selected every 9–10 days to minimize the variation in the view angles.

calibration of Band 1 and transfer of the calibration by the glint reflection. Due to the uncertainty in the water vapour absorption in Band 2, the error in the calibration of Band 2 relative to Band 1 is ± 5 per cent, which is about a half of the total range of the water vapour absorption. The r.m.s. error increases to ± 12 per cent and ± 7 per cent, for the absolute error and precision respectively. The effect of changes in the aerosol burden, and in the illumination and view directions on desert calibration are discussed in appendix A2. The precision of the calibration over deserts in Band 1 is computed as the square root of the sum of squares of the individual errors (± 4 per cent for aerosols, ± 1 per cent for view angle and ± 2 per cent for solar zenith angle). Placing limits of <2 per cent on the standard deviation relative to the mean

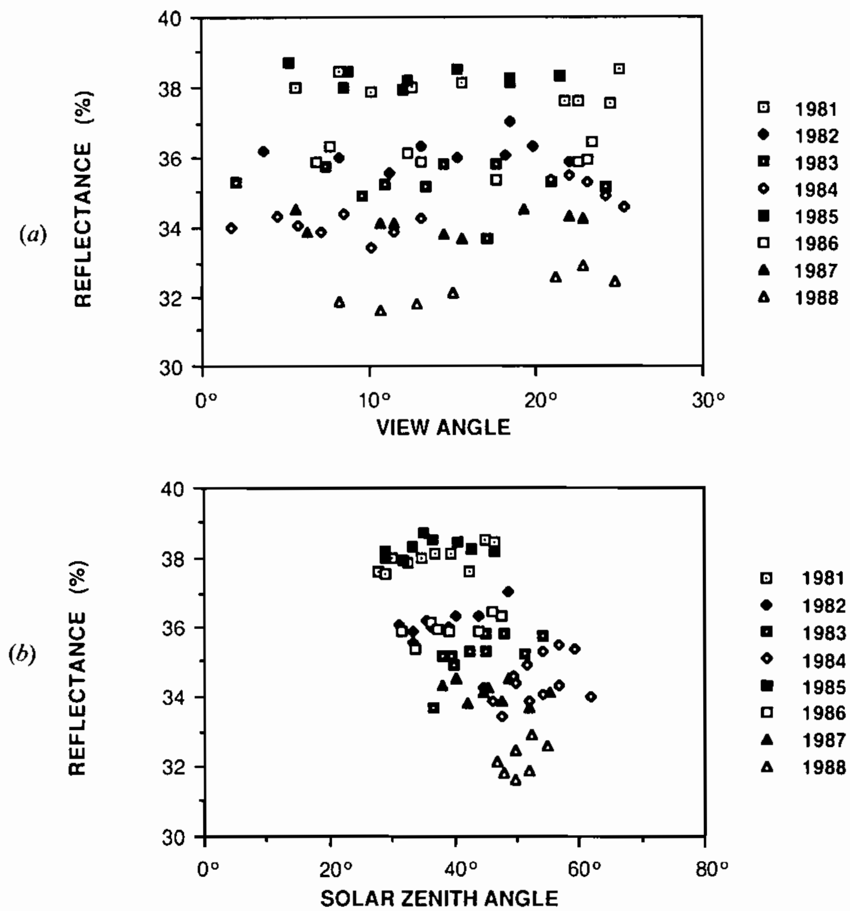

Figure 7. The dependence of the reflectance of the Egyptian desert (area no. 2) in Band 1 on the view zenith angle (*a*) and on the solar zenith angle (*b*). The figure shows that there is a large overlap in the range of view angles (solar zenith angles) between data from the different years. As a result the systematic variation in the solar zenith angle from year to year, due to a drift in the satellite equatorial crossing time, cannot explain the difference in the reflectance measured over the two desert areas.

for selecting data at a particular observation time and site reduces the error. The uncertainty in Band 2 is slightly higher due to variations in water vapour absorption. The differences in the calibration between the four sites were smaller than ± 3 per cent, which is considered as the precision error.

3. Results

The desert calibration was applied to four desert sites in the north of the Sahara. Two over south-west Libya, centred at 25·5° N, 14° E and 25° N, 12° E and two on the Egyptian-Libyan border, centred at 29° N, 25° E and 26·5° N and 26° E. These desert areas are very dry in August and September and devoid of vegetation, therefore, its reflectance is constant in time. The areas selected for the calibration are easily identified by their brightness and uniformity and the histograms of their reflectance showed small and stable standard deviations through time. The ocean areas were chosen over the Indian Ocean, north-west of Australia, around 110° E and 10° S, as well as over the Pacific Ocean around 160° E and 10° S. The ocean calibration was chosen in the Southern hemisphere, in the vicinity of Australia, since the area is relatively pollution free (Weller and Leiterer 1988), far from sources of dust, smoke or anthropogenic pollution (as over the Atlantic). In these latitudes the aerosol optical thickness is around 0·1 in the visible part of the spectrum (Weller and Leiterer 1988). Similar values ($0{\cdot}1 \pm 0{\cdot}1$) are reported from the NOAA remote sensing data of oceanic aerosol optical thickness (Rao *et al.* 1988 and 1989), which includes the ocean calibration sites. Aerosol optical thicknesses were measured at Cape Grim, representing background conditions. The range of the optical thickness during 1985 was 0·03–0·10 for 500 nm and 675 nm (Forgan and Fraser 1987). It is expected that in the equatorial latitudes, where the ocean calibration was performed, the aerosol optical thickness is slightly higher than the average value of 0·07 measured in Cape Grim.

3.1. *Ocean calibration*

An example of the calibration applied to Band 1 a short time after the launch of NOAA-9 (December 1984) and three years later (in December 1987) is shown in figure 8 (*a*). The solid line represents the theoretical fit to the experimental points (+) using the calibration coefficients supplied by NOAA. The slope of the least square fit between the theoretical and the measured radiances (see figure 8 (b)) is the calibration ratio, r_i, defined in (4). As described before, the glint, due to its wavelength independent reflectivity, was used to 'transfer' the calibration from Band 1 to Band 2. The calibration was applied to ocean images from August 1981 to February 1988. About 10 images, that were found to be relatively cloud-free, were selected each year (out of 50–100 screened images per year). Table 3 presents the results of the ocean calibration. Note that the data are usually from August to December, except for 1984 and 1987 where the data extends to January 1985 and February 1988 respectively. In figure 9 the calibration ratio derived from the ocean data are plotted. The bars in the figure are the standard deviation of the calibration ratio between the different images. The calibration coefficient α in units of $\mathrm{W\,\mu m^{-1}\,st^{-1}\,m^{-2}}$ per count was computed from the calibration ratio (see appendix A1) and tabulated with calibrations reported in the literature in table 4. The results are compared with the NOAA high flying aircraft calibration (Whitlock *et al.* 1988, Smith *et al.* 1987, 1988) and with calibration over the White Sands (Teillet *et al.* 1988, 1990 and Frouin and Gautier 1987). There is a good agreement between the present ocean calibration and the Aircraft NOAA calibration for 1986 (within the calibration errors), but not for 1985. There is also a good agreement with the results of Teillet *et al.* (1990) for 1987 and 1988 (note that the ocean calibration for 1987 was performed between August 1987 and February 1988, and therefore falls between the calibration of Teillet *et al.* in 1987 and 1988). In this respect it should be noted that in the comparison between different calibration methods presented by Whitlock *et al.* (1988), there was a large difference between the NOAA calibration and the other calibration methods for 1985.

3.2. *Desert calibration*

An example for the calibration procedure applied to the desert areas for NOAA-7 and -9 is shown in figure 10. The reflectances of the Egyptian desert in area 2, obtained without consideration for the change in the calibration, are plotted in

(a)

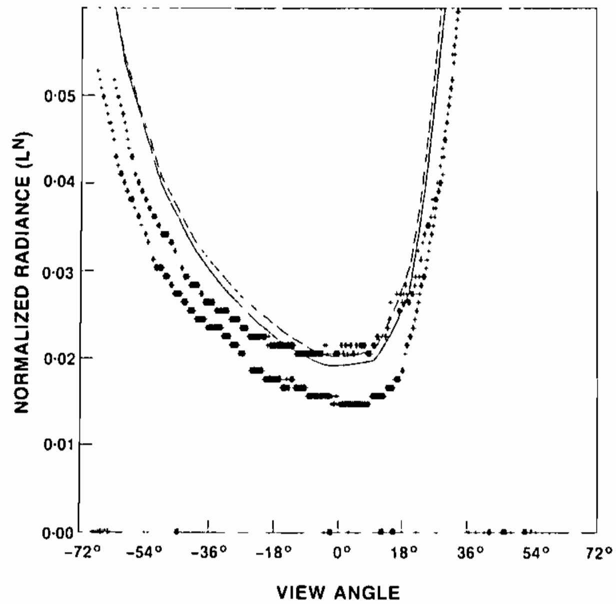

(b)

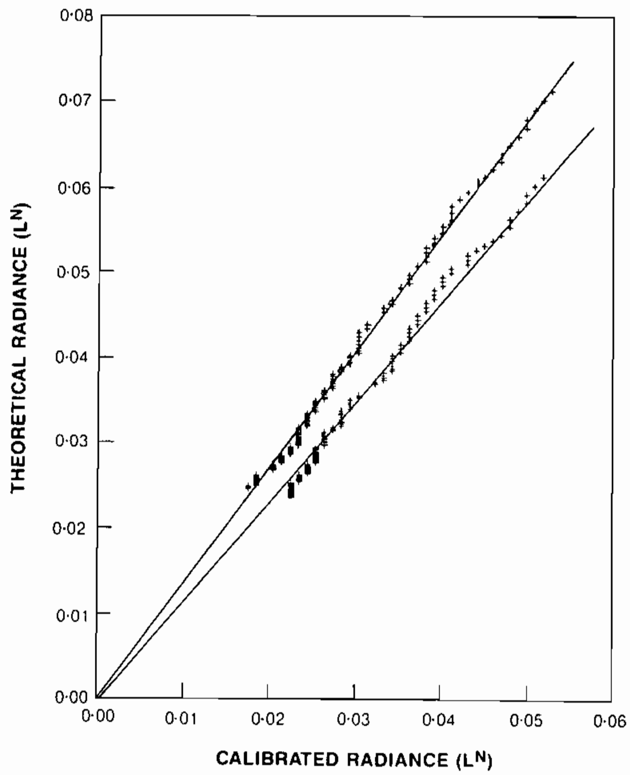

Figure 8. (*a*) The normalized radiance, in Band 1, detected by the satellite using the calibration provided on the tape (+) and the model predictions (solid and dashed lines). Data are compared between the early operation of NOAA-9 (29 December 1984—dashed line) and three years later (30 December 1987—solid line). The data are plotted as a function of the view angle for azimuth of 175° (for the negative view angles), showing the deterioration of the sensor response. (*b*) The relation between the theoretical radiance predicted from the model and the normalized radiance calibrated by the calibration coefficients given on the tape. A linear relation between the two radiances is found. The measured radiances are lower by 14 per cent than the predicted radiances for 1984 and 26 per cent for 1987.

Table 3. Calibration change of AVHRR-7, -9 and -11 for Bands 1 and 2. The results are given for the ocean calibration and for the desert calibration. The uncertainty in the calibration, in this table, represents the standard deviation between the different cases used to compute each value. NOAA changed the calibration coefficients on the level 1B tapes on 27 September 1990. This accounts for the large increase in γ and α between 1990 and 1991. Using the original calibration coefficients for 1991 γ becomes 0·80 and 0·69 for channel 1 and 2 respectively.

	Calibration ratio (r)			
Year	Ocean Band 1	Ocean Band 2	Desert Band 1	Desert Band 2
NOAA-7				
1981	0·84±0·02	0·77±0·04	0·91±0·01	0·87±0·01
1982	0·88±0·02	0·80±0·04	0·87±0·01	0·80±0·01
1983	0·91±0·04	0·84±0·01	0·84±0·01	0·83±0·01
1984	0·90±0·03	0·86±0·05	0·81±0·01	0·75±0·01
NOAA-9				
1885	0·87±0·03	0·82±0·03	0·92±0·01	0·86±0·01
1986	0·87±0·05	0·82±0·05	0·87±0·00	0·82±0·00
1987	0·08±0·07	0·81±0·07	0·82±0·01	0·80±0·01
1988			0·78±0·02	0·78±0·02
NOAA-11				
1989			0·79±0·01	0·68±0·01
1990			0·80±0·02	0·68±0·01
1991			0·83±0·02	0·75±0·01

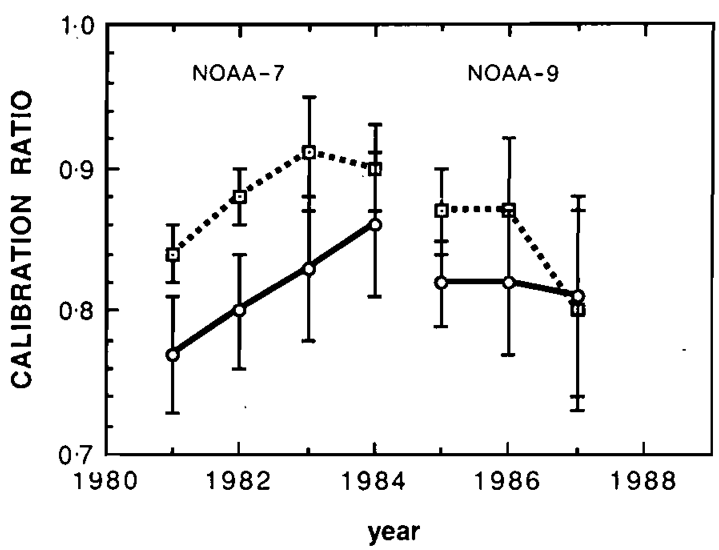

Figure 9. The calibration ratio, based on the ocean calibration for Band 1 (·······) and Band 2 (——). The bars represent the standard deviation between about ten analysed images every year.

Table 4. Comparison between the calibration coefficient α($W\,\mu m^{-1}\,st^{-1}\,m^{-2}$/count) of the NOAA-7, -9 and -11 AVHRR sensor calibration as measured by the present method over the ocean and deserts, and other methods (after Whitlock *et al.* 1988 except of the results of Teillet *et al.* 1990). The preflight values from Teillet *et al.* (1988) are shown as well as the calibration given by NOAA on the magnetic tapes.

		NOAA preflight		Present calibration		NOAA aircraft		
Year	Band	Tapes	(Teillet *et al.* 1988)	Ocean	Desert	Smith *et al.* (1987, 1988)	Teillet *et al.* (1990)	Frouin and Gautier
NOAA-7								
	1	0·56	0·53	0·66±0·03	0·62±0·02			
1981	2	0·35	0·35	0·46±0·04	0·40±0·02			
	1	0·56	0·53	0·64±0·03	0·65±0·02			
1982	2	0·35	0·35	0·44±0·04	0·44±0·02			
	1	0·56	0·53	0·62±0·04	0·67±0·02			
1983	2	0·35	0·35	0·43±0·05	0·45±0·02			
	1	0·56	0·53	0·62±0·03	0·69±0·02			
1984	2	0·35	0·35	0·41±0·05	0·47±0·02			
NOAA-9								
	1	0·55	0·52	0·62±0·06				
1984–1985	2	0·36	0·33	0·42±0·06				
	1	0·55	0·52	0·63±0·03	0·60±0·02	0·53±0·03	0·55	0·58
1985	2	0·36	0·33	0·44±0·04	0·42±0·02	0·36±0·02	0·39	0·37
	1	0·55	0·52	0·63±0·05	0·63±0·02	0·60±0·03	0·73	0·62
1986	2	0·36	0·33	0·44±0·05	0·44±0·02	0·41±0·02	0·48	0·39
	1	0·55	0·52	0·69±0·07	0·67±0·02		0·67	
1987	2	0·36	0·33	0·44±0·07	0·45±0·02		0·44	
	1	0·55	0·52		0·71±0·02	0·65±0·03	0·71	
1988	2	0·36	0·33		046±0·02	0·42±0·02	0·46	
NOAA-11								
	1	0·47			0·60±0·02			
1989	2	0·28			0·41±0·02			
	1	0·47			0·59±0·02			
1990	2	0·28			0·41±0·02			
	1	0·49			0·59±0·02			
1991	2	0·30			0·41±0·02			

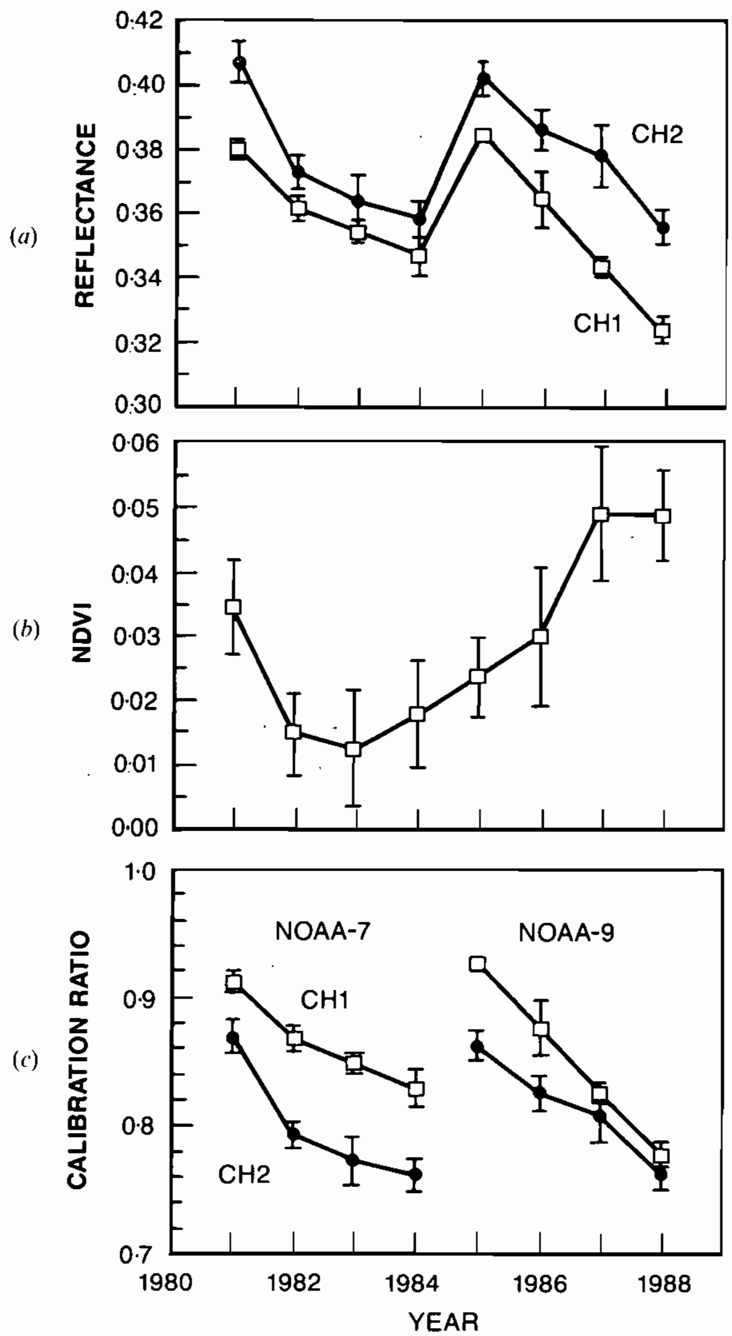

Figure 10. Example of analysis of the desert data. (*a*) The reflectance of the Egyptian desert (area no. 2) as a function of the year for the two bands. The error bars show the standard deviation between reflectances collected from about 10 days in August and September each year. The calibration deterioration results in the apparent changes of the reflectance, and the apparent increase of the reflectivity with the switch to the new satellite. (*b*) The vegetation index (NDVI) obtained from the data of (*a*) as the ratio of the difference in the reflectance in Band 2 and Band 1 divided by their sum. The wrong calibration introduces apparent change in the NDVI of 0·04. (*c*) The calibration ratio (defined as the ratio between the radiance calibrated with the preflight calibration and the true radiance) derived from the data over the Egyptian desert (area no. 2), assuming that the desert reflectivity was constant in time and using the calibration over the ocean for 1986 as an anchor point.

figure 10 (*a*). The corresponding vegetation index is shown in figure 10 (*b*). It is seen that without the calibration correction, the desert reflectance changes substantially in time, with substantial difference in the vegetation index, which may be interpreted as changes in the vegetation cover or other surface characteristics. In order to find the calibration change, we need to assume that the desert reflectivity is not changing in time, and that we know the actual calibration in one particular instance. The small variation of the desert reflectance during 40–70 days each year, shown in figure 6, is used as the basis for this assumption. The agreement between the NOAA aircraft calibration, the present ocean calibration in 1986 (within the experimental accuracy—see table 4), the ocean calibration, and the results of Teillet *et al.* (1990) in 1987 and 1988, suggests the use of ocean calibration for 1986 and 1987 as anchor points for the desert calibration. The results of the calibration are shown in figure 10 (*c*). The same procedure was applied to all four desert areas, resulting in the calibration ratio shown in figures 11 (*a*) and 11 (*b*) for the two AVHRR bands. The results from all four sites agree very well with each other (within an uncertainty smaller than ± 2 per cent), therefore the assumption of a constant desert reflectance is consistent between the four desert sites. The calibration coefficient recovered in 1985 after the satellite replacement (NOAA-7 to NOAA-9), to almost the same value as in the early stage of NOAA-7. For NOAA-11 the calibration ratio (table 3) did not recover with the replacement of NOAA-9 with NOAA-11, though the calibration coefficient α did recover (table 4). The values of the calibration ratio and the standard deviations between the four sites are tabulated in table 3, and compared with the calibration ratio, derived from the ocean calibration. In figure 11 (*c*) and figure 12, the results of the ocean calibration and the desert calibration are compared. The differences in the calibration ratio between Band 1 and Band 2 (figure 11 (*c*)) are similar for the two calibration methods during the whole calibration period. The values of the calibration ratio derived for each band (figure 12) by the two methods is similar for NOAA-9 but substantially different for NOAA-7. These differences are discussed in the next section. The calibration coefficients α_i were computed from the calibration ratio (r_i) (see appendix A1) and tabulated in table 4.

4. Discussion of the calibration results

The results of the calibration for NOAA-7, NOAA-9 and NOAA-11 by the ocean and desert methods were given by the ratio of the preflight calibration to the true calibration in table 3 and figures 11 and 12, and by the calibration coefficient α_i in table 4. Both methods agreed on calibration deterioration for NOAA-9 of 10 ± 3 per cent in Band 1 and 16 ± 2 per cent in Band 2 a short time after Launch, and 22 ± 1 per cent in both bands three years later. The two methods differed in the calibration values for NOAA-7 as is dramatically emphasized in figure 12. Instead of a decrease in the sensor sensitivity of 10 per cent in Band 1 and 12 per cent in Band 2, as predicted by the desert calibration method for the life time of the satellite, the ocean calibration indicates an increase of 6 per cent in Band 1 and 9 per cent in Band 2 for the same period. The difference between the calibration in the two bands was found to be similar in the two methods (see figure 11). For NOAA-11 the desert calibration indicates a decrease in the sensor sensitivity of 21 ± 3 per cent in Band 1 and 33 ± 3 per cent in Band 2 three months after the launch. Deterioration of the sensor of 1·5 per cent and 2 per cent in the two bands respectively was measured during the next year till February 1990. Note that the value of α for the NOAA-11

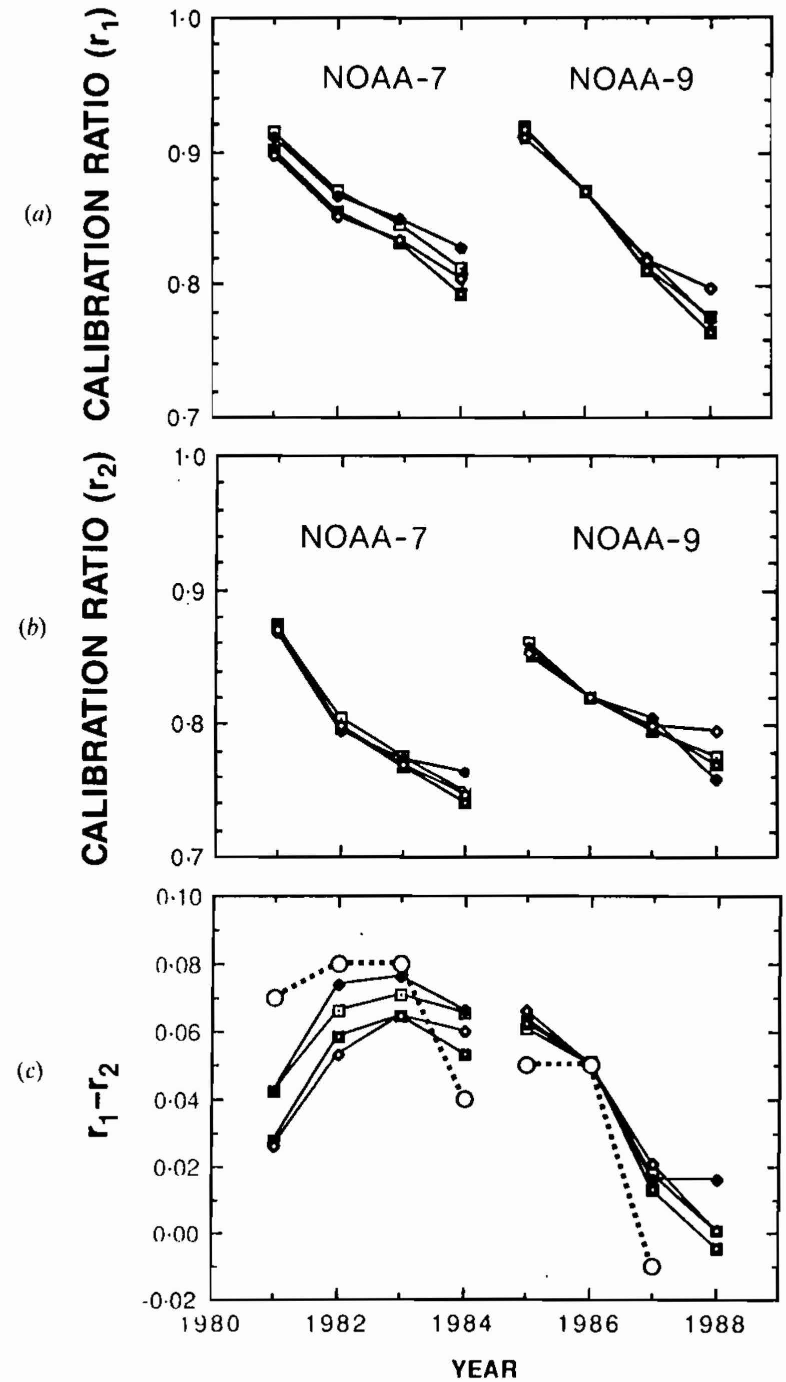

Figure 11. The calibration ratio (defined as the ratio between the radiance calibrated with the preflight calibration and the true radiance) from the four desert sites as a function of the year for NOAA-7 and NOAA-9, for Bands 1 (*a*) and Band 2 (*b*). The difference between the calibration ratio in the two bands is also plotted (solid lines) (*c*) and compared with the results from the ocean method (···O···).

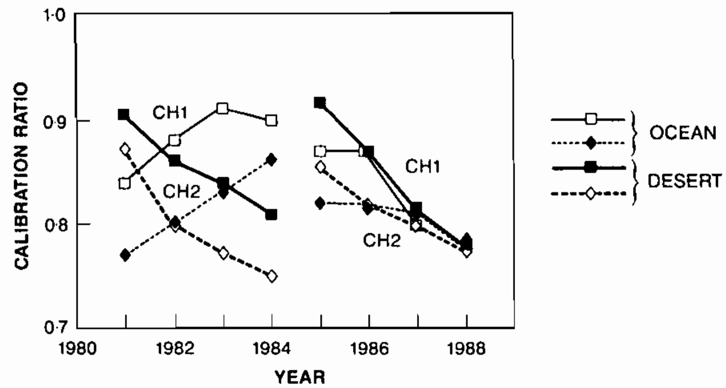

Figure 12. Comparison between the average calibration ratio derived over the desert and the calibration ratio derived over the ocean for Band 1 (solid lines) and Band 2 (dashed lines).

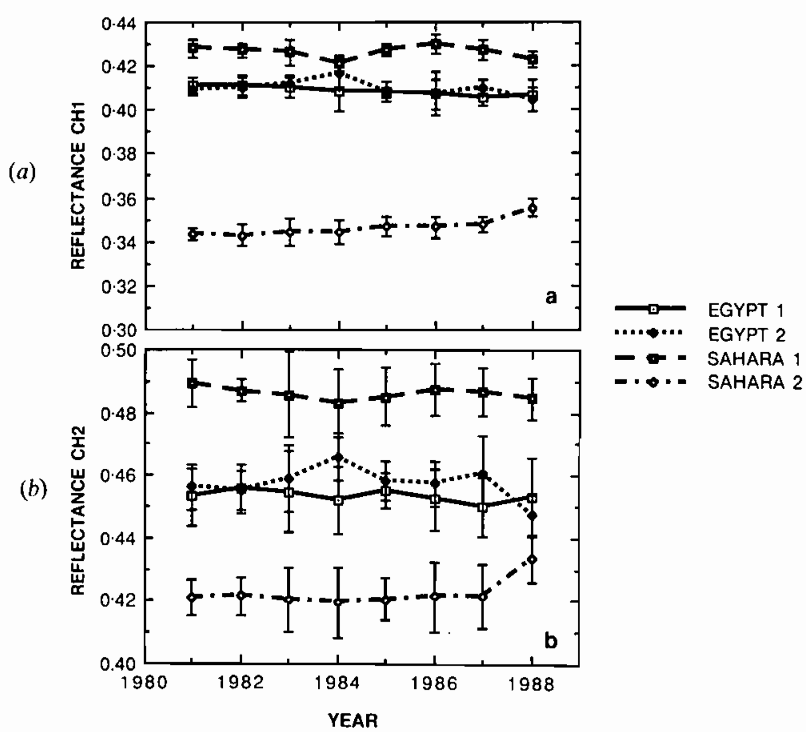

Figure 13. The reflectance of the four desert sites in Band 1 (*a*) and in Band 2 (*b*), based on the desert reflectance after the new satellite calibration was applied.

sensor after launch (table 4) is similar to the value for NOAA-9 and NOAA-7 directly after launch. Therefore the large difference between the preflight calibration and the inflight calibration of NOAA-11 may be not due to deterioration of the sensor, but rather due to inadequacy of the preflight calibration.

Possible reasons for the difference between the results of the two methods for NOAA-7 should be looked for in the specific characteristics of each of the methods, as summarized below:

1. *Precision*. The desert calibration is more precise than the ocean method, due to the stability of the desert surface and the small effect of changes in the atmospheric composition on the upward radiance above the bright desert areas (much smaller than above the dark ocean—for the effect of the atmosphere above dark and bright surfaces see Fraser and Kaufman 1985). Therefore, systematic increases in the aerosol optical thickness over the ocean areas, during the NOAA-7 operation could result in an apparent increase in the sensor sensitivity.
2. *Wavelength response*. The desert reflectivity is relatively wavelength independent. The Egyptian desert reflectance changes from 0·41 in Band 1 to 0·45 in Band 2 (see figure 13). Ocean calibration in Band 1 is based on molecular scattering that is strongly weighted to the short wavelengths (molecular scattering is inversely proportional to the fourth power of the wavelength). The transfer of the calibration from Band 1 to Band 2 over the ocean is based on the glint reflection which is, again, wavelength independent. If the sensor spectral response varied in time during the operation of NOAA-7, due to deterioration of the interference filters or due to condensation of outgassed substances on the optical instruments, then the calibration coefficients *should* be different for these spectrally different calibration methods. Channel 1 would have a different calibration using the desert calibration or the molecular scattering calibration, while the difference between the calibration of the two bands would be similar in the desert and glint calibrations (both are insensitive to the spectrum of the radiation). For NOAA-9, different sensor characteristics may result in a stable wavelength response and in better similarity between the different calibration methods. A decrease of 10 nm in the effective wavelength of the spectral band, (e.g. from 0·63 μm to 0·62 μm) would result in an increase in the detected radiance (in Band 1) over the ocean by 5 per cent and a decrease of 0·5 per cent in the radiance over the desert.
3. *Linearity*. The molecular calibration method tests the calibration procedures over the lower end of the calibration curve (for radiance range of 0·02–0·09 in reflectance units), while the glint transfer of calibration and the desert calibration is applied to a higher range of radiances (0·1–0·4). The detector was tested before the flight and was found to be linear, and a linear relationship was found in figure 8 between the deep space values and the ocean calibration. If, despite these facts, the sensor linearity was damaged for NOAA-7, it may explain the differences in the calibration results.

It is concluded that the differences between the two methods of calibration for NOAA-7 are not necessarily due to inherent inaccuracies in one of the methods, but rather may be due to some changes in the sensor characteristics, in addition to a general degradation in the response. To fully answer this question, there is a need for a detailed study of the hypothetical sensor behaviour, as well as to test the ocean and desert calibration methods on additional, independent sites. There is also a need to apply the calibration to sites with different spectral response (e.g., forests and snow). Future aircraft calibration efforts, such as the one by Smith *et al.* (1988) are recommended to be performed not only over the 'White Sands', but also over surface covers with different spectral reflectance (both magnitude and wavelength dependence). Meanwhile, the higher precision of the desert calibration, and the neutral spectral reflectance of the desert makes it a better candidate for the calibration choice. As a result, the recommendations for the AVHRR calibration, given in §6, are based on absolute calibration using the ocean method for 1986, and using the desert calibration for monitoring changes in calibration between 1981 and 1990.

Instrument polarization effects were not included in this investigation, however a brief discussion is in order. The net effect of instrument polarization is equal to the product of the percentage instrument polarization, percentage source polarization and the percentage of the total signal that may be polarized. The AVHRR polarization sensitivity is approximately 4 and 5 per cent for Bands 1 and 2 at all view angles (ITT 1982). The ocean calibration requires modeling Rayleigh scattering and ocean glint radiances both of which polarize light up to 65 and 100 per cent respectively in channel 1 and 45 and 100 per cent in the near-IR. The percentage of total signal for off-nadir due to molecular scattering is 77 and 62 per cent for channels 1 and 2 respectively and for glint 85 and 92 per cent (table 1). Assuming the worst case for molecular scattering in channel 1, the radiance would be underestimated for Rayleigh scattering by 2 per cent ($0{\cdot}04 \times 0{\cdot}65 \times 0{\cdot}77 = 0{\cdot}020$) which is well within our precision. The Sun glint error is 3·4 per cent ($0{\cdot}04 \times 1{\cdot}00 \times 0{\cdot}85 = 0{\cdot}034$) in channel 1 and 4·6 per cent ($0{\cdot}05 \times 1{\cdot}00 \times 0{\cdot}92 = 0{\cdot}046$) in channel 2. The desert radiance is not polarized, and therefore is not affected by the instrument polarization. Since these values are also within our limits of precision and their magnitudes are nearly the same, polarization should have a negligible effect on the transfer of calibration from channel 1 to 2. We do not believe polarization considerations are required in evaluating the ocean and desert methods at this time.

5. Applications

In this section we shall apply the derived calibration to several remote sensing problems and test the implications of the calibration deterioration. Suggestions for simple correction schemes for NDVI values reported in numerous previous studies are given.

5.1. *Desert reflectivity*

The calibration is applied to the same desert reflectance data which were used in the calibration process itself. The calibration was derived from the average of the reflectances measured above four desert sites. The application of the calibration to each site separately, can indicate the stability of the reflectance of that site relatively to the average of all the sites. The resultant reflectances are shown in figure 13. The reflectance of the Egyptian desert area #1 was found to be the most stable one. In the Egyptian desert area #2 the reflectance apparently increased in 1984 in both bands by 0·01 and was reduced by similar amount in 1988. In 1988 we also see an increase of 0·01 in the reflectance of the Sahara desert area #2. These increases and decreases of 0·01 in the reflectance are within the standard deviation of the reflectances themselves in the period of time of observation (a few weeks every year), but they show that precise calibration over the desert, in a similar way performed in the present work (possibly with more desert sites), can be used to detect small changes in the environment. Without the calibration, the desert reflectances (ρ) showed variations of $\Delta\rho = 0{\cdot}12$ and it was impossible to resolve between long term changes in the environment (of the order of 10 years) and the satellite calibration.

5.2. *Vegetation dynamics*

The visible and near-IR bands of the AVHRR are used by many investigators to monitor land processes such as vegetation dynamics (typically in the form of a ratio) over large areas due to the satellites coarse resolution and high temporal frequency. The ratio is then related to a biotic activity such as gross primary productivity (Prince 1988) or it maybe used in a classification algorithm to distinguish and monitor distinct cover types through time. Lack of calibration could seriously compromise the temporal utility of these data. An example of this is the NOAA global vegetation index data set in which the 10-day composite NDVI is formed from the individual bands producing a 25 km resolution image for the world. We reformed an African continental subset from the NOAA uncalibrated data to our calibrated (hereafter referred to as NASA calibrated) data for September composites in 1982, 1983 and 1984, retaining also the single band values. The purpose of the present application is to find the error which is introduced by the calibration degradation. In table 5 results are shown for the difference between the uncalibrated values and the NASA calibration for the reflectance in the visible and near-IR, and the NDVI images for the three years in question. The differences in the visible and near-IR bands are stratified according to cover type, desert areas having the greatest difference (4 to 5 per cent for Band 1 and 6 to 7 per cent for Band 2) and vegetated areas having small differences (1 to 2 per cent for Band 1 and 2 to 5 per cent for the near-IR band, table 5). These figures show the difference to be a function of the cover type and generally increase with aging of the satellite.

Three observations of the NDVI response to calibration are noteworthy. The absolute calibration increases the NDVI by an average of 0·040 for the years in question. The NDVI difference varies slightly with cover type varying from a mean of 0·041 for deserts to 0·038 for forests. The year to year variation in the difference due to instability in the calibration is small and would depend on the cover type.

Table 5. Calibration effect on reflectance and NDVI: The difference (reflectance with preflight calibration—reflectance with NASA calibration) for Band 1 and Band 2, and the NDVI for three years of the NOAA-7 global vegetation index (GVI) product.

	Reflectance difference								
	CH1			CH2			ΔNDVI		
	1982	1983	1984	1982	1983	1984	1982	1983	1984
Desert	0·044	0·047	0·052	0·063	0·069	0·073	0·038	0·045	0·041
Forest	0·016	0·019	0·018	0·036	0·039	0·037	0·036	0·048	0·030

Table 6. NDVIs calculated from normalized (N) radiances and apparent (A) radiances for three simulated cover types and one observed desert site. The average ΔNDVI can be used as an approximate correction to NDVIs generated from uncorrected NOAA-7, -9 and -11 AVHRR data.

	1981	1982	1983	1984	1985	1986	1987	1988	1989	1990
Dense green biomass $\rho_1^N=0{\cdot}100$ $\rho_2^N=0{\cdot}200$ $NDVI^N=0{\cdot}333$										
$NDVI^{NA}$	0·303	0·242	0·285	0·240	0·305	0·315	0328	0·337	0·246	0·243
ΔNDVI	0·030	0·042	0·048	0·043	0·029	0·019	0·005	0·004	0·087	0·091
Low green biomass $\rho_1^N=0{\cdot}200$ $\rho_2^N=0{\cdot}250$ $NDVI^N=0{\cdot}111$										
$NDVI^{NA}$	0·085	0·073	0·066	0·071	0·0782	0·093	0·109	0·119	0·023	0·019
ΔNDVI	0·026	0·038	0·045	0·040	0·029	0·018	0·003	0·008	0·088	0·092
No green biomass $\rho_1^N=0{\cdot}410$ $\rho_2^N=0{\cdot}460$ $NDVI^N=0{\cdot}058$										
$NDVI^{NA}$	0·031	0·019	0·012	0·016	0·027	0·039	0·054	0·064	−0·027	−0·031
ΔNDVI	0·026	0·038	0·045	0·041	0·031	0·019	0·004	−0·007	0·085	0·088
Egypt site (Desert, 1986 data) $\rho_1^N=0{\cdot}41$ $\rho_2^N=0{\cdot}46$ $NDVI^N=0{\cdot}058$										
$NDVI^{NA}$	0·035	0·015	0·013	0·017	0·023	0·028	0·048	0·048	−0·015	−0·005
ΔNDVI	0·023	0·043	0·045	0·041	0·035	0·030	0·010	0·010	0·073	0·063
Average										
ΔNDVI	0·026	0·040	0·046	0·041	0·031	0·021	0·006	−0·002	0·087	0·090
s.d.	±0·002	±0·002	±0·001	±0·001	±0·002	±0·005	±0·003	±0·007	±0·001	±0·002

5.3. *Correction of NDVIs from previous studies*

In the following we shall examine whether previous NDVI values, computed in numerous studies have to be recomputed from raw data or if a simple correction scheme is possible. This question is approached by simulating the relation between a given spectral reflectance ρ_i^N and the apparent normalized spectral reflectance ρ_i^{NA} (normalized to reflectance units- $\rho=L^N/\cos\theta_0$) based on the preflight calibration. This was completed for targets having a high green biomass density, low green biomass density and no green biomass. Results are presented in table 6 along with actual observations taken from one of the desert sites. The simulation shows relatively small variations in NDVI ($\Delta NDVI$) between cover types and good agreement between the simulated data and the Egyptian Desert site data. The time dependence of $\Delta NDVI$ ranges from 0·03 in 1981, 0·05 in 1983 to near 0·00 in 1988 and up again to 0·09 in 1990. These data also agree very well with the data in the previous example. Therefore it is suggested that an approximate NDVI correction is possible for historical NDVI that is largely independent of cover type and is given by the average NDVIs in table 6. It should be noted that due to the error of ±5 per cent in the transfer of calibration between the two channels by the ocean glint, the absolute error in $\Delta NDVI$ is about ±0·02 and the precision error is ±0·02.

5.4. *Calibration effect on biomass yield*

Calibration affects gross biomass production estimates based on AVHRR NDVI. From Prince (1991), the relation between gross production and the NDVI is:

$$\text{Gross production} = ek\sum_t a(\text{NDVI}_t - r_t)S_t$$

where:

e is the growth efficiency term,
k is the energy equivalent of dry plant material 16·8 Kj/g for herbs (Leith, 1968),
$NDVI_t$ is the normalized difference vegetation index during time interval t,
r_t indicates the effect of the vegetation background on the NDVI,
S_t is the global photosynthetically active radiation incident during time interval t,
a is a function relating NDVI to per centage absorbed photosynthetically active radiation and is approximately equal to 1 (Goward and Dye 1987).

Using the NASA calibrated radiances resulted in variation of the biomass yield of 365 g m^{-2} in the Sahel between 1981 and 1988. Radiances computed from the uncorrected preflight calibration result in biomass yield of 257 g m^{-2}, or a change of 30 per cent in the worst case for low biomass. The high biomass case indicates a decrease of 11 per cent from the NASA to the preflight calibration. The above method relating satellite radiances to biotic production has been extended to define regions of biotic activity and has been suggested by Dregne and Tucker (1988) as a possible approach to define desert boundaries particularly when applied to multi-year data. They reported results in terms of integrated NDVI (days) of which the 6–8 day interval corresponds closely to the limit of the agroclimatic semiarid zone. They noted that this band shifted 200 km south in Niger, Sudan and Chad from 1981 (a sufficiently wet year) to 1984 (a very dry year). Improper calibration reduces the number of NDVI days by ~2·2 between 1981 and 1984, which would effectively move the boundary into an 8–10 NDVI day biological productivity zone. This does not invalidate Dregne and Tucker's results as they include calibration changes in their results.

5.5. *Remote sensing of oceanic aerosol*

Some investigators are using the AVHRR Band 1 data to derive the aerosol optical thickness over the oceans (Rao *et al.* 1988, 1989). For an ocean reflectance of 1 per cent in AVHRR Band 1 (underwater reflectance and surface reflectance) for nadir viewing, an observed calibrated radiance for an aerosol optical thickness of $\tau_a = 0{\cdot}40$ would be interpreted with the preflight calibration in 1984 as $\tau_a = 0{\cdot}24$. Many other applications could be addressed, however all strongly suggest that a calibration is required to accurately understand the research being conducted.

6. Calibration summary and comparison

The time dependence of the calibration of the AVHRR visible and near-IR channels, is based on the reflected radiance from the four desert sites, and the deep space values. The absolute calibration is based on the ocean method applied to data from 1986. The results show an average deterioration of the sensor sensitivity in channel 1 of $3{\cdot}8 \pm 1{\cdot}6$ per cent per year for NOAA-7, $5{\cdot}7 \pm 1{\cdot}0$ per cent per year for NOAA-9 and 1 per cent for NOAA-11. The deterioration of NOAA-7 and -9 is in agreement with the results of Staylor (1990) of 3·5 per cent and 6 per cent respectively, and larger than the 0 per cent for NOAA-7 and 4·4 per cent for NOAA-9 of Brest and Rossow (1990). In figure 14 (a) the results of the present desert calibration for the AVHRR Bands 1 and 2 are shown for 1981–1990. Analytical linear or parabolic fits to the calibration ratio (r) were computed (solid lines for Band 1 and dashed for Band 2) resulting in:

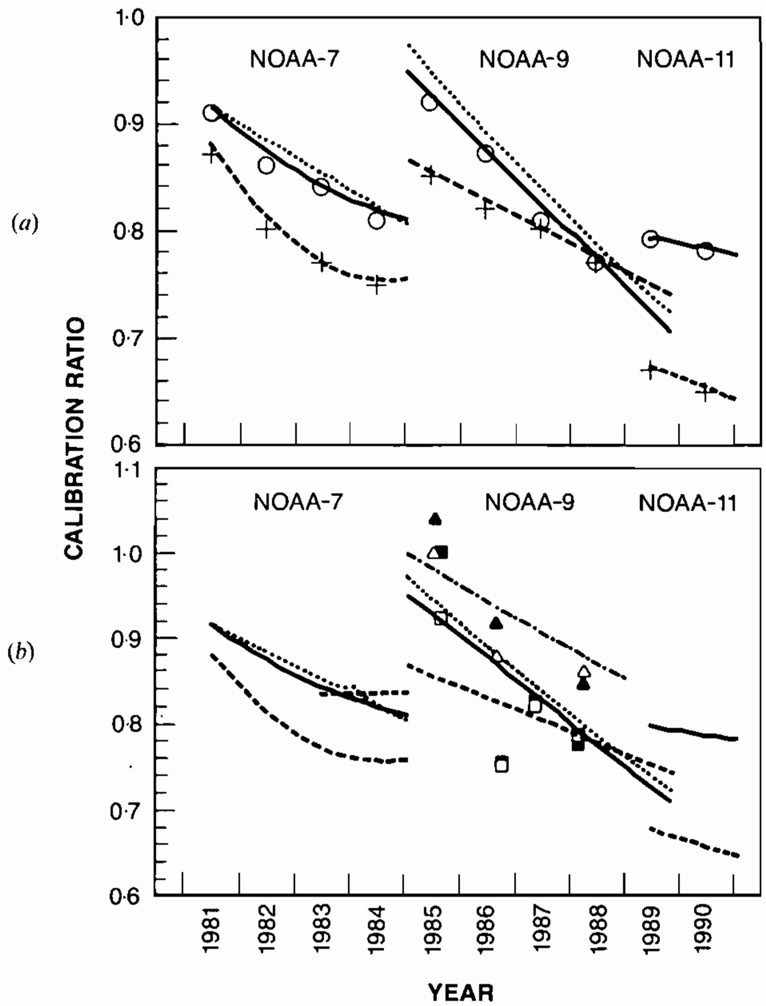

Figure 14. (*a*) Summary of the calibration ratio for Bands 1 and 2 for NOAA-7, -9 and -11, derived from the desert calibration. (○)—Band 1, (+)—Band 2, the solid and dashed lines, show the analytical fit to the points (given by (5)) for Bands 1 and 2 respectively. The dotted line represents the calibration of Staylor (1990) for Band 1, anchored to the present value in 1981. (*b*) Comparisons between the results of the present desert calibration for Bands 1 and 2 (solid and dashed lines respectively), the calibration of Staylor (1990—dotted line), the NOAA U-2 calibration (Smith *et al.* 1987, 1988—Δ, ▲ in Bands 1 and 2), the calibration of Teillet *et al.* (1990—□ ■ in Bands 1 and 2), and the calibration of Brest and Rossow (1990—dashed lines, in Band 1).

$$r_1 = 0{\cdot}916 - 0{\cdot}049(Y - 1981{\cdot}5) + 0{\cdot}0050(Y - 1981{\cdot}5)^2 \quad \text{for NOAA-7} \quad (5a)$$

$$r_2 = 0{\cdot}882 - 0{\cdot}080(Y - 1981{\cdot}5) + 0{\cdot}0125(Y - 1981{\cdot}5)^2 \quad \text{for NOAA-7} \quad (5b)$$

$$r_1 = 0{\cdot}953 - 0{\cdot}051(Y - 1985) \quad \text{for NOAA-9} \quad (5c)$$

$$r_2 = 0{\cdot}866 - 0{\cdot}026(Y - 1985) \quad \text{for NOAA-9} \quad (5d)$$

$$r_1 = 0{\cdot}797 - 0{\cdot}010(Y - 1989) \quad \text{for NOAA-11} \quad (5e)$$

$$r_2 = 0{\cdot}683 - 0{\cdot}020(Y - 1989) \quad \text{for NOAA-11} \quad (5f)$$

Here Y is the year given on a continuous scale, so that 1 April 1985 will be 1985·25.

Our results are compared in figure 14 (a) with calibration deterioration equations given by Staylor (1990) for Band 1. For purposes of comparison, Staylor's calibration was anchored to the present calibration in 1981, since it is a relative calibration. The trends of the calibration deterioration are very similar in both cases. In figure 14 (b) the calibration equations (5) and Staylor's calibration are compared with the calibration of Smith *et al.* (1987, 1988), Teillet *et al.* (1990) and Brest and Rossow (1990). It is seen that the calibration values of Teillet *et al.* (1990) fit the present results for 1987 and 1988 within 0–2 per cent, but deviates for 1985 and 1986. The results of Brest and Rossow (1990) did not capture the 3·5 per cent deterioration in the system response from 1983 to 1984, shown by the present results and these of Staylor (1990), and show a smaller degradation for NOAA-9.

Acknowledgment

We would like to thank Ginny Kalb and Shana Matto for writing the software that was used for the data analysis; Bob Fraser, Bruce Guenther, Brian Markham, John Price and Jim Tucker for helpful discussions and for reviewing the manuscript and a special thanks to Gilli Joseph and Jackie Kendall for extracting the data.

Appendix (details of the caibration algorithm

A1. Algorithm for calibration over the oceans

Over the oceans the calibration is performed by a comparison between the detected radiances and the theoretical predictions. The theoretical radiances are computed by the radiative transfer code developed by Ahmad and Fraser (1982). In this code the radiance in a plane parallel atmosphere is simulated, taking into account the polarization of the radiation and the true angular dependence of the ocean reflectance matrix for a given wind speed. The underwater reflectance was assumed to be 0·003 in Band 1 and 0·0 in Band 2. The aerosol optical thicknesses are 0·1 for band 1 and 0·008 for Band 2, which fits a maritime aerosol model used before (Fraser and Kaufman 1986). The gaseous absorption is 0·04 for Band 1 (mainly due to ozone absorption) and 0·10 for Band 2 (mainly due to water vapour absorption). The gaseous absorption was computed by the LOWTRAN code (Kneizys *et al.*, 1983) for the AVHRR spectral filters. In order to define the aerosol and molecular scattering properties, and represent properly the molecular scattering, that provides 75 per cent of the radiance, the effective wavelength was defined for each band as:

$$\lambda_0 = \frac{\int_0^\infty \lambda F_o(\lambda) f(\lambda) \lambda^{-4} \mathrm{d}\lambda}{\int_0^\infty F_o(\lambda) f(\lambda) \lambda^{-4} \mathrm{d}\lambda} \tag{A1}$$

where $F_o(\lambda)$ is the solar spectral irradiance, $f(\lambda)$ is the spectral response of the sensor and λ^{-4} is the spectral dependence of the molecular optical thickness (Rayleigh 1871). The radiative transfer computations are performed for λ_o and results in the normalized radiance (L^N), given in (2). The AVHRR counts were converted for convenience to reflectance units as well by the calibration given on the magnetic tape. The detected radiances, in reflectance units (after the data screening process described in §2.2) are plotted as a function of the theoretical radiances (e.g., figure 9).

The slope of the least square linear fit to this plot (r_1) is the ratio between the radiance (in reflectance units) obtained from the AVHRR raw counts with the calibration on the magnetic tape and the true radiance (in reflectance units). Examples of the results are given in table 3. The slope r_1 is therefore, the correction that should be applied to the reflectance obtained from the calibrated image. The calibration coefficient α_i is computed from the value of r_i in (4), and γ_i in (3):

$$\alpha_i = \gamma_i(\text{preflight})\, E_{oi} d^2/(\pi r_i) \tag{A 2}$$

The solar fluxes, integrated on the NOAA-7, -9 and -11 response functions are given by Price (1987 b, 1988 and Planet 1988):

$E_{01}(\text{NOAA-7}) = 1649\,\text{W m}^{-2}\,\mu\text{m}^{-1}$ and $E_{02}(\text{NOAA-7}) = 1040\,\text{W m}^{-2}\,\mu\text{m}^{-1}$

$E_{01}(\text{NOAA-9}) = 1629\,\text{W m}^{-2}\,\mu\text{m}^{-1}$ and $E_{02}(\text{NOAA-9}) = 1043\,\text{W m}^{-2}\,\mu\text{m}^{-1}$

$E_{01}(\text{NOAA-11}) = 1630\,\text{W m}^{-2}\,\mu\text{m}^{-1}$ and $E_{02}(\text{NOAA-11}) = 1053\,\text{W m}^{-2}\,\mu\text{m}^{-1}$

The values were scaled for the solar irradiance of Neckel and Labs (1981), based on the relation of the Neckel and Labs and Thekaekara's values given by Price (1988) for NOAA-10.

The calibration coefficients given by NOAA are:

$\gamma_1(\text{NOAA-7})100 = 0{\cdot}1068$ $\gamma_2(\text{NOAA-7})100 = 0{\cdot}1069$

$\gamma_1(\text{NOAA-9})100 = 0{\cdot}1063$ $\gamma_2(\text{NOAA-9})100 = 0{\cdot}1075$

$\gamma_1(\text{NOAA-11})100 = 0{\cdot}0906$ $\gamma_2(\text{NOAA-11})100 = 0{\cdot}0835$

A2. Simulations of the satellite sensor response due to expected uncertainties in the calibration method over deserts

To calibrate the AVHRR visible and near-IR bands over desert areas requires that several criteria be met or assumed regarding the site and the satellite/target/Sun geometry. First the area must be large with respect to the spatial resolution of the satellite (4 km at nadir for the AVHRR GAC proposed for this study) and registration inaccuracies ($\pm$ one pixel for AVHRR GAC), therefore a minimum target size of 16 km is required to repetitively locate the same pixel characteristics. Our preliminary investigations suggest that statistical information over the sites is useful in screening for cloud and dust contamination therefore a much larger sample is required, approximately 100 km square from which a subsample will be extracted.

Large calibration sites demand that their reflectance properties and the optical properties of the over laying atmosphere be uniform spatially and temporally. Spatial uniformity of the site and atmosphere is reliably checked by examining the standard deviation of the radiance over the site. Our preliminary work suggests that standard deviations greater than 2 per cent of the site mean radiance should be rejected. The reflectance of the site and atmosphere therefore had to be spatially uniform.

Temporal uniformity for the desert surface requires that no vegetation or soil moisture be present during the observation period, the surface be geologically stable and that cultural influences be absent. Likewise the atmosphere should be relatively free of clouds, dust outbreaks and anthropogenic aerosols. Since this proposed work lacks a field programme component, temporal stability can only be monitored by close examination of the temporal satellite data over desert sites that meet the above criteria. In addition, desert areas all over the world will be chosen in order to reduce

Table A1. The influence of desert aerosols on satellite level reflectances for AVHRR Band 1. Simulations using the radiative transfer code of Ahmad and Fraser (1982) for view angle (ϕ) = 0° solar zenith angle (θ) = 30° and surface reflectance $\rho = 0{\cdot}4$.

	Aerosol optical thickness				
	0·0	0·2	0·4	0·7	1·0
L/F	0·3377	0·3256	0·3132	0·2954	0·2793

L/F = level reflectance.

the probability of a climatological or geological change affecting all of the sites. The importance of the desert aerosols may be seen in table A1 An uncertainty of 0·2 in aerosol optical thickness causes a change of ± 4 per cent in the radiance measured by the AVHRR Band 1. Similar values are expected for Band 2. Additionally water vapour absorption in this band will most influence temporal comparisons owing to temporal changes in atmospheric water vapour. Site selection must be restricted to regions removed from strong influences of water vapour fluxes.

The view angle and solar zenith angle can change by approximately seven and four degrees respectively across the large calibration sites proposed for this study. Likewise the satellite position at the times of observation for the Saharan sites introduces a variation of 10° in view angle if we limit our observations to the nine-day orbit repeat cycle and a change of 16° in solar zenith angle during the proposed August and September observation period. Additionally a slow increase in the solar zenith angle of $5°/\mathrm{yr}^{-1}$ occurs due to a lengthening of the local time of equitorial crossing of 0.5 $\mathrm{hr/yr}^{-1}$. These geometric variations further require the calibration sites to be nearly isotropic scatters for the pertinent geometry of this study.

As an example of the importance of an isotropic surface, we have simulated the radiance at the top of the atmosphere from a Lambert surface reflector of 0·4, an aerosol optical thickness of 0·2, solar zenith angle of 30°, an aerosol size distribution expected for desert aerosols for AVHRR Band 1 for three view angles 0°, 30° and 60°, table A2 For forward scattering viewing from 0° to 60° in the principal plane. The simulated radiance decreases by only 4 per cent. A 10° change in view angle such as we would expect in this study causes a < 1 per cent decrease. The effect of

Table A2. Simulation of satellite level reflectance using the radiative transfer code of Ahmad and Fraser (1982) for Saharan aerosol optical thickness of 0·2 and viewing in the principal plane in the forward scatter direction.

Satellite level reflectance and % change from nadir			
ρ/satellite view angle	0°	30°	60°
0·4	0·326/0%	0·316/−3%	0·311/−4%
Satellite level reflectance and % change from solar zenith angle of 20°			
ρ/satellite view angle	0°	30°	60°
0·4	0·384/0%	0·376/−2%	0·370/−4%
Satellite level reflectance for various suface reflectance			
satellite view angle/ρ	0·25	0·40	0·60
30°	0·204	0·316	0·311/−4%

changing the solar zenith angle by 20° reduces the exoatmospheric reflectance by only 2 per cent for this simulation. Should the surface be anisotropic the resultant satellite level radiances are roughly proportional to the surface bidirectional reflectance for these conditions and would yield highly variable results limiting its usefulness for calibration. Simulations for AVHRR near-IR are similar.

A search of the deserts of the Americas and Africa have yielded two regions in the Sahara which are adequate for this research. Site selection will continue for Asia and Australia.

References

ARKING, A., and CHILDS, J., 1985, Retrieval of cloud cover parameters from multispectral satellite images. *Journal of Climate and Applied Meteorology*, **24**, 322–333.

AHMAD, Z., and FRASER, R. S., 1982, An iterative radiative transfer code for ocean-atmosphere system. *Journal of Atmospheric Science*, **39**, 656–665.

BREST, C. L., and ROSSOW, W. B., 1990, Radiometric calibration and monitoring of NOAA AVHRR visible data. *7th Conference of Atmospheric Radiation* (Boston, MA: AMS), pp. 68–74.

DINER, D. J., and MARTONCHIK, J. V., 1985, Atmospheric transmittance from spacecraft using multiple view angle imagery. *Applied Optics*, **23**, 3503–3511.

DREGNE, H. E., and TUCKER, C. J., 1988, Green biomass and rainfall in Semi-arid sub-Sahara Africa. *Journal of Arid Environments*, **15**, 245–252.

FORGAN, B. W., and FRASER, P. J., 1987, Baseline atmospheric program (Australia) 1985, Department of Science, Cape Grim, Australia.

FRASER, R. S., and KAUFMAN, Y. J., 1985, The relative importance of scattering and absorption in remote sensing. *I.E.E.E. Transactions on Geoscience and Remote Sensing*, **23**, 625–633.

FRASER, R. S., and KAUFMAN, Y. J., 1986, Calibration of satellite sensors after launch. *Applied Optics*, **25**, 1177–1185.

FROUIN, R., and GAUTIER, C., 1987, Calibration of NOAA-7 AVHRR, GOES-5 and GOES-6 VISSR/VAS solar bands. *Remote Sensing of Environment*. **22**, 73–101.

GOWARD, S. N., and DYE, D. G., 1987, Evaluating North American net primary productivity with satellite data. *Advances in Space Research*, **7**, 165–174.

HOLBEN, B. N., 1986, Characteristics of maximum value composite images for temporal AVHRR data. *International Journal of Remote Sensing*, **7**, 1417–1437.

HOLBEN, B. N., and FRASER, R. S., 1984, Red and near-IR sensor response to off-nadir viewing. *International Journal of Remote Sensing*, **5**, 145–160.

HOLBEN, B. N., KAUFMAN, Y. J., and KENDALL, J. D., 1990, NOAA-11 AVHRR visible and near-IR calibration. *International Journal of Remote Sensing*, **11**, 1511–1519.

ITT AEROSPACE, 1982, AVHRR/2 Advanced Very High Resolution Radiometer Technical Description, ITT Aerospace/Optical Division, NASA Contract No. NAS5-26771, Fort Wayne, Indiana 46801.

JURSA, A. S., editor, 1985, Handbook of Geophysics and Space Environment, AFGL Air Force System Command, ADA 167000, National Technical Information Series, Springfield, VA.

KAUFMANN, Y. J., 1984, Atmospheric effects on remote sensing of surface reflectance. *Proceedings of the Society of Photo-optical Instrumental Engineering*, **475**, 20–33.

KAUFMAN, Y. J., and SENDRA, C., 1988, Algorithm for atmospheric corrections of visible and near-IR satellite imagery. *International Journal of Remote Sensing*, **9**, 1357–1381.

KAUFMAN, Y. J., HOLBEN, B. N., KENDALL, J. D., and MEKLER, Y., 1990, Inflight calibration of the NOAA-AVHRR visible and near-IR chanels. *IGARSS Symposium Washington, D.C.*, (New Jersey: I.E.E.E. Inc.), pp. 511–514.

KOEPKE, P., 1982, Vicarious satellite calibration in the solar spectral range by means of calculated radiances and its application to Meteosat. *Applied Optics*, **21**, 2845-2855.

KNEIZYS, F. X., SHETTLE, E. P., GALLEXY, W. O., CHETWYND, J. H., ABREU, L. W., SELBY, J. E. A., CLOUGH, S. A., and FENN, R. W., 1983, Atmospheric transmittance/Radiance: Computer code LOWTRAN6. AFGL, Hanscom, AFB MA 01731.

LEITH, H., 1968, The measurement of calorific values of biological material and the determination of ecological efficiency. In *Functioning of Terrestrial Ecosystems at the Primary Production Level*, edited by F. E. Eckardt (Paris: United Nations Educational, Scientific and Cultural Organization).

NECKEL, H., and LABS, D., 1981, Improved data of solar spectral irradiance from 0·33 to 1·25. *Solar Physics*, **74**, 231–249.

PLANET, W.G., editor, 1988, Data extraction and calibration of TIROS-N/NOAA radiometers, NOAA Technical Memorandum NESS 107-Rev. 1, Appendix B.

PRICE, J. C., 1987a, Radiometric calibration of satellite sensors in the visible and near-IR: history and outlook. *Remote Sensing of Environment*, **22**, 3–9.

PRICE, J. C. 1987b, Calibration of satellite radiometers and the comparison of vegetation indexes. *Remote Sensing of Environment*, **21**, 15–27.

PRICE, J. C., 1988, An update on visible and near IR calibrations of satellite instruments. *Remote Sensing of Environment*, **24**, 419–422.

PRINCE, S. D., 1991, A model of regional primary production for use with coarse resolution satellite data, *International Journal of Remote Sensing*, **12**, 1313–1330.

RAO, C. R. N., STOWE, L. L., MCCLAIN, E. P., and SAPPER, J., 1988, Development and application of aerosol remote sensing with AVHRR data from the NOAA satellite. In *Aerosol and Climate*, edited by P. V. Hobbs, M. P. McCormick (Hampton, Virginia: Deepak), pp. 69–79.

RAO, C. R. N., STOWE, L. L., and MCCLAIN, E. P., 1989, Remote Sensing of aerosol over ocean using AVHRR data, theory, practice and application. *International Journal of Remote Sensing*, **10**, 743–749.

RAYLEIGH, LORD (J. W. Strutt), 1871, Light from the sky, its polarization and colour, *Philosophical Magazine*, **41**, 107–120.

SMITH, G. R., LEVIN, R. H., ABEL, P., and JACOBOWITZ, H., 1987, Calibration of the solar bands of the NOAA-9 AVHRR and GOES-6 VISSR using high altitude aircraft measurements. *Presented in the International Union of Geodesy and Geophysics, Vancouver, Canada.*

SMITH, G. R., LEVIN, R. H., ABEL, P., and JACOBOWITZ, H., 1988, Calibration of the solar bands of the NOAA-9 AVHRR using high altitude aircraft measurements. *Journal of Atmosphere and Ocean*, **5**, 631–639.

STAYLOR, W. F., 1986, Site selection and directional models of desert used for ERBE validation targets. NASA TP-2540.

STAYLOR, W. F., 1990, Degradation rates of the AVHRR visible channel for the NOAA-6, -7 and -9 Spacecraft. *Journal of Atmosphere and Ocean*, **7**, 411–423.

TEILLET, P. M., SLATER, P. N., MAO, Y., DING, Y., BARTELL, R. J., BIGGAR, S. F., SANTER, R. P., JACKSON, R. D., and MORAN, M. S., 1988, Absolute radiometric calibration of the NOAA AVHRR sensors. *Society of Photo-optical Instrument Engineers Conference, Orlando, Florida, April, 1988. Society of Photo-optical Instrument Engineers*, **924**, 196–207.

TEILLET, P. M., SLATER, P. N., MAO, Y., DING, Y., BARTELL, R. J., BIGGAR, S. F., SANTER, R. P., JACKSON, R. D., and MORAN, M. S., 1990, Three methods for the absolute calibration of the NOAA AVHRR sensors in flight. *Remote Sensing of Environment*, **31**, 105–120.

TUCKER, C. J., TOWNSHEND, J. R. G., and GOFF, T. E., 1985, African land cover classification using satellite data. *Science, New York*, **227**, 369–375.

WELLER, M., and LEITERER, U., 1988, Experimental data on spectral aerosol optical thickness and its global distribution. *Beiträge zur Physik der Atmosphäre*, **61**, 1–9.

WHITLOCK, C. H., STAYLOR, W. F., SMITH, G., LEVIN, R., FROUIN, R., GAUTIER, C., TEILLET, P. M., SLATER, P. N., KAUFMAN, Y. J., HOLBEN, B. N., ROSSOW, W. B., BREST, C., and LECROY, S. R., 1988, AVHRR and VISSR satellite instrument calibration results for both cirrus and marine stratocumulus IFO periods. FIRE Science Team Meeting, Vail, Colorado.